



Universiteit
Leiden
The Netherlands

Paving the path between low- and high-mass star formation : dynamics probed by Herschel far-infrared spectroscopy

San Jose Garcia, I.

Citation

San Jose Garcia, I. (2015, June 18). *Paving the path between low- and high-mass star formation : dynamics probed by Herschel far-infrared spectroscopy*. PhD Thesis. Retrieved from <https://hdl.handle.net/1887/33224>

Version: Not Applicable (or Unknown)

License: [Licence agreement concerning inclusion of doctoral thesis in the Institutional Repository of the University of Leiden](#)

Downloaded from: <https://hdl.handle.net/1887/33224>

Note: To cite this publication please use the final published version (if applicable).

Cover Page



Universiteit Leiden




The handle <http://hdl.handle.net/1887/33224> holds various files of this Leiden University dissertation

Author: San José García, Irene

Title: Paving the path between low- and high-mass star formation : dynamics probed by *Herschel* far-infrared spectroscopy

Issue Date: 2015-06-18



*Infall versus turbulence as the origin
of sub-millimetre line broadening
in protostellar envelopes:
from low- to high-mass*

*I. San José-García, J. C. Mottram, E. F. van Dishoeck, et al.
submitted*

Abstract

The analysis of spectrally resolved molecular line observations is a powerful tool to characterise the dynamical structure of protostellar environments. Previous studies of young stellar objects (YSOs) based on data from ground-based single-dish telescopes have been restricted to the outer colder parts of their envelopes. However, *Herschel* has revealed the dynamical properties of inner warmer regions, giving further insights into the complete understanding of the star formation process, for both low- and high-mass YSOs.

As part of the “Water In Star-forming regions with *Herschel*” (WISH) survey, we quantify the contributions of infall and turbulence to the broadening of low- and high- J $C^{18}O$ and HCO^+ line profiles for a sample of low- and high-mass YSOs across a wide luminosity range (from <1 to $>10^5 L_{\odot}$).

Optically thin $C^{18}O$ $J = 3-2$, $9-8$ and $10-9$ and optically thick HCO^+ $J = 4-3$ and $J = 6-5$ spectra are modelled with the non-LTE radiative transfer code `RATRAN`. An iterative method is used to constrain the infall and turbulent velocities, and abundance profiles which best-fit all the observed lines.

Both turbulence and infall are necessary to reproduce the $C^{18}O$ and HCO^+ observations simultaneously. The pure infall dominated scenario is excluded for all studied YSOs, while pure turbulent dominated models are ruled out for the majority. The turbulent width increases with the luminosity of the source and is significantly higher in the protostellar phase compared to that observed in pre-stellar cores. For the low-mass protostars, the observed broadening of higher- J $C^{18}O$ transitions can be explained by including infall motions but not by adding a gradient in turbulence. For most of the massive YSOs, the best-fit infall component is slower than the maximum infall velocity estimated from their assumed stellar masses. The infall velocity seems to increase with luminosity for massive sources above $\sim 10^3 L_{\odot}$ and is independent of L_{bol} below this value. In addition, most of these massive objects show slightly larger values of turbulent velocity than those calculated for systems in virial equilibrium, implying that, even if the star initially forms from a quasi-virial equilibrium core, turbulence prevails over the gravitational potential once star formation is underway. Finally, a jump abundance profile is needed for all YSOs to reproduce the $C^{18}O$ observations, whereas a constant profile is sufficient for HCO^+ .

Turbulence in protostellar envelopes increases significantly from the pre-stellar to protostellar phase regardless of mass. This suggests that a source of turbulence, such as outflows, switches on during the star formation process. The dynamical properties in the inner warm regions of high-mass protostellar envelopes, closer to the actual forming star, could be considered scaled-up version of their low-mass counterparts.

3.1. Introduction

One of the challenges in star formation is to uncover the links between the star formation process for low and high-mass young stellar objects (YSOs). The dynamical conditions of their environments are tightly related to the formation and evolution of YSOs, so the study of their velocity fields provides insight into the existing similarities and differences between low- and high-mass star forming regions.

The classical low-mass star formation scenario must be modified to explain the formation of massive stars due to their different radiative pressure, formation timescales, accretion rates, stronger radiation feedback and injected energy by powerful outflows and companions (Zinnecker & Yorke 2007). The various scenarios describing the high-mass star formation process imply different levels of turbulence dominating their cores and different infall velocities (see McKee & Tan 2002, 2003; Bonnell & Bate 2005; Hocuk & Spaans 2010; Krumholz & Bonnell 2009). In addition, infall and rotation come into play affecting parameters such as accretion rate, degree of turbulence, outflow force, etc. (Behrend & Maeder 2001b). Therefore, understanding the dynamical properties of YSO environments, especially in their pre-stellar and early embedded phase, is a crucial component of a global theory capable of explaining how stars form irrespective of their final masses.

A powerful tool used to disentangle the complexity of these objects is molecular spectroscopy. Spectrally resolved lines characterise the conditions in different components of protostellar environments as well as their dynamical structure. In particular, CO and its isotopologues play a pivotal role in tracing different physical components within the protostar and providing information about gas motions. ^{12}CO is used to observe the entrained material in the outflow while optically thin C^{18}O mostly probes quiescent envelope gas.

With the available ground-based telescopes, most CO studies have been limited to low- and intermediate- J transitions (J up to 6–5). These lines probe the colder outer part of protostellar environments ($>10^3$ and $>10^4$ AU for low- and high-mass objects respectively). However, the Heterodyne Instrument for the Far-Infrared (HIFI; de Graauw et al. 2010) on board the *Herschel*¹ Space Observatory (Pilbratt et al. 2010), has enabled spectrally resolved observations of high- J CO transitions (up to $J = 16$ –15), probing the higher densities closer to the protostar and resolving the velocity components traced by the warm gas. HIFI observations of molecular lines are unique as they probe frequency ranges not observable from the ground with unprecedented sensitivity and spectral resolution. More importantly, these observed transitions allow us to extend the comparison between low- and high-mass YSOs to parts of the protostar which are an order of magnitude closer to the actual forming star (e.g. Yıldız et al. 2010; Plume et al. 2012; San José-García et al. 2013).

Within the context of the “Water In Star-forming regions with *Herschel*” Guaranteed Time Key Programme (WISH; van Dishoeck et al. 2011), San José-García et al. (2013) presented a study of the low- and high- J transitions of ^{12}CO , ^{13}CO and C^{18}O for a sample of 51 embedded YSOs covering a range of luminosities from <1 to $>10^5 L_{\odot}$. They investigated the dynamics of the entrained outflowing and envelope material on scales of 10^2 – 10^3 AU and 10^3 – 10^4 AU for low- and high-mass YSOs respectively, by decomposing the ^{12}CO and C^{18}O line profiles into different Gaussian components. The entrained gas in the outflow causes broad line-wings in the ^{12}CO spectra, while non-thermal motions in the envelope broaden and shape the C^{18}O profiles. Understanding the motions in the envelopes of low and high-mass YSOs will reveal whether these processes are independent of the luminosity of the central protostar.

In order to characterise the dynamical structure of protostellar envelopes, the first step is to analyse the four non-thermal motions that can contribute to the velocity field: turbulence, infall, expansion, and rotation. Emission generated by turbulent motions is characterised by symmetric Gaussian profiles such as those observed for C^{18}O , C^{17}O and discussed in Jørgensen et al. (2002) for low-mass YSOs. The observational signature of infalling gas is a blue-shifted asymmetric double-peaked line (Myers et al. 1996). This specific profile is observed only if the line is optically thick (see Evans 1999), because in the optically thin case the absorption feature is not produced

¹*Herschel* is an ESA space observatory with science instruments provided by European-led Principal Investigator consortia and with important participation from NASA.

and the line profile remains symmetric. For this reason, infall motions need to be studied with optically thick emission lines using molecules such as HCO^+ (Gregersen et al. 1997, Hogerheijde et al. 1999, Fuller et al. 2005), a well known infall tracer in protostellar envelopes. Expansion creates similarly skewed line profiles as those generated by infall motions but with a red-shifted asymmetry, so these two motions can be differentiated. On the other hand, rotation is not characterised by a unique distinctive profile since it can generate both red and blue asymmetric lines on either side of the rotation axis. Rotation generally becomes important on small scales ($<1000\text{AU}$, Brinch et al. 2007, 2009). Given the need to resolve the region in order to characterise rotation, this is more of an issue for interferometric studies.

In this paper, we will study the dynamical structure of protostellar envelopes as a function of luminosity by constraining the contributions of turbulence and infall on single-dish C^{18}O and HCO^+ line profiles. For this purpose, we model the $\text{C}^{18}\text{O } J = 3-2, J = 9-8, J = 10-9$ and $\text{HCO}^+ J = 4-3, J = 6-5$ spectra of 14 YSOs with 1-D spherically symmetric non-LTE radiative transfer models, varying the degree of turbulence and infall motions. An overview of the studied sample and observations is presented in Sect. 3.2. The radiative transfer models, input parameters, abundance profiles and fitting technique are explained in Sect. 3.3. The turbulent and infall velocities from the best-fit models and possible alternative scenarios describing the dynamics in the envelopes are presented in Sect. 3.4. Then, in Sect. 3.5 we discuss the implications of these results and finally, in Sect. 3.6 the conclusions are summarised.

3.2. Observations

3.2.1. Sample

The sample for this study consists of 14 YSOs from the WISH survey which are detected in $\text{C}^{18}\text{O } J = 9-8$ and $10-9$, and for which $\text{HCO}^+ J = 4-3$ observations are available. These sources are classified into two groups according to their bolometric luminosities, L_{bol} : five low-mass protostars, characterised by $L_{\text{bol}} < 40 L_{\odot}$, and nine high-mass YSOs with $L_{\text{bol}} > 2 \times 10^3 L_{\odot}$. In addition, the high-mass sub-sample of YSOs contains a mix of evolutionary stages, including hot cores, mid-IR quiet and ultracompact HII regions. However, the number of sources of each type is too small to reach statistically significant conclusions, so we instead focus the study on the covered luminosity range. The observed characteristics of each source are discussed in van der Tak et al. (2013) for the high-mass, and Yıldız et al. (2013) for the low-mass protostars.

Table 3.1 presents the bolometric luminosities of the sample members, the distances (d), galactic radii (R_{GC}), source velocities (v_{LSR}), envelope masses (M_{env}) and $^{16}\text{O}/^{18}\text{O}$ isotopic ratio calculated from the relation found by Wilson & Rood (1994), in which the ratio scales with the R_{GC} of the source. Also given is the stellar mass, M_* , which is calculated for the high-mass young stars by assuming that the massive sources are on the main sequence and by using the conversion from Table 1 of Mottram et al. (2011). For the low-mass protostars, an initial stellar mass of $1 M_{\odot}$ is used to constrain the maximum infall velocity. The actual stellar mass is determined from the best-fit of the infall velocity during the fitting procedure (see Sect. 3.3.3). For more information about the sample studied in WISH see van Dishoeck et al. (2011).

3.2.2. C^{18}O observations

The $\text{C}^{18}\text{O } J = 9-8$ and $10-9$ spectra used in this paper were observed with the HIFI instrument for the entire WISH sample of YSOs. These transitions were detected for all high-mass objects but only for five low-mass protostars. As mentioned in Sect. 3.2.1, we could not use the entire WISH sub-sample of high-mass YSOs because the $\text{HCO}^+ J = 4-3$ transition was available for only nine out of the 19 massive objects. More information about the characteristics of the HIFI C^{18}O observations, observation techniques, data reduction procedure and empirical line decompositions are given in San José-García et al. (2013).

Table 3.1: Bolometric luminosity, spectral type, mass of the central forming star, distance, galactocentric radius, velocity, envelope mass, and $^{16}\text{O}/^{18}\text{O}$ isotopic ratio of the studied low- and high-mass YSOs.

Source	L_{bol} (L_{\odot})	M_{*}^a (M_{\odot})	d (kpc)	R_{GC}^b (kpc)	v_{LSR} (km s^{-1})	M_{env}^c (M_{\odot})	$^{16}\text{O}/^{18}\text{O}^d$
Low-mass							
NGC1333 IRAS 2A	35.7	≤ 1	0.235	8.7	7.7	5.1	549 ± 131
NGC1333 IRAS 4B	4.4	≤ 1	0.235	8.7	7.1	3.0	549 ± 131
SMM1	30.4	≤ 1	0.415	8.3	8.5	16.1	525 ± 128
GSS30 IRS1	13.9	≤ 1	0.125	8.4	3.5	0.6	529 ± 128
Elias 29	14.1	≤ 1	0.125	8.4	4.3	0.3	529 ± 128
High-mass							
IRAS05358+3543	6.3×10^3	10.7	1.8	10.3	-17.6	142	642 ± 146
NGC6334-I(N)	1.9×10^3	7.4	1.7	6.8	-4.5	3826	437 ± 115
DR21(OH)	1.3×10^4	13.3	1.5	8.4	-4.5	472	531 ± 129
W3-IRS5	1.7×10^5	35.3	2.0	10.0	-38.4	424	624 ± 143
IRAS18089-1732	1.3×10^4	13.3	2.3	6.3	33.8	172	406 ± 111
W33A	4.4×10^4	20.2	2.4	6.2	37.5	700	401 ± 110
IRAS18151-1208	2.0×10^4	15.3	3.0	5.7	32.0	153	374 ± 106
G10.47+0.03	3.7×10^5	50.2	5.8	3.1	67.0	1168	217 ± 90
G34.26+0.15	3.2×10^5	46.4	3.3	6.1	57.2	1792	393 ± 109

Notes. See van Dishoeck et al. (2011) and van der Tak et al. (2013) for the source coordinates and references regarding distance and bolometric luminosity values of the low- and high-mass YSOs, respectively.

^(a) The assumed maximum stellar mass for all low-mass protostars is $1 M_{\odot}$. For the high-mass YSOs, M_{*} has been calculated using the assumptions presented in Mottram et al. (2011). ^(b) The galactocentric radii were calculated using distances d in this table and the IAU distance from the galactic centre $R_{\odot} = 8.5$ kpc. ^(c) For the low-mass protostars, the envelope masses are determined by Kristensen et al. (2012) within the radius at which the dust temperature reaches 10 K. For the high-mass objects, this parameter is taken from van der Tak et al. (2013). ^(d) Expected $^{16}\text{O}/^{18}\text{O}$ isotope ratios calculated using the equation on Wilson & Rood (1994): $^{16}\text{O}/^{18}\text{O} = (58.8 \pm 11.8)R_{\text{GC}} + (37.1 \pm 82.6)$.

Complementing the HIFI data, $\text{C}^{18}\text{O } J = 3-2$ spectra were obtained with the James Clerk Maxwell Telescope² (JCMT) on Mauna Kea, Hawaii, and the Atacama Pathfinder EXperiment telescope³ (APEX) on Llano de Chajnantor, Chile. In the case of the JCMT data, jiggle maps observations were obtained with the Heterodyne Array Receiver Programme (HARP; Buckle et al. 2009). The spatial resolution at that frequency is $\sim 14''$ and the spectral resolution for the studied sources is 0.1 km s^{-1} . Each map was convolved to $20''$ and the central spectrum was extracted and re-binned to 0.27 km s^{-1} . A more detailed description of the APEX data and the low- J C^{18}O transitions for the low-mass protostars can be found in Yıldız et al. (2013).

The upper-level energies (E_u), rest frequencies of the transitions, telescope, main beam efficiencies (η_{MB}), beam sizes and spectral resolutions for all studied C^{18}O observations are presented in Table 3.2.

3.2.3. HCO^{+} observations

Together with the C^{18}O observations, $\text{HCO}^{+ } J = 4-3$ and $6-5$ spectra are included in the analysis with the aim of restricting the parameter that describes the infall motions in the inner and outer regions of protostellar envelopes. The $\text{HCO}^{+ } J = 6-5$ transition was observed together with

²The James Clerk Maxwell Telescope is operated by the Joint Astronomy Centre on behalf of the Science and Technology Facilities Council of the United Kingdom, the National Research Council of Canada, and (until 31 March 2013) the Netherlands Organisation for Scientific Research.

³APEX is a collaboration between the Max-Planck-Institut für Radioastronomie, the European Southern Observatory, and the Onsala Space Observatory.

Table 3.2: Overview of the main properties of the observed C^{18}O and HCO^+ lines. For a description of the parameters see Sect. 3.2.2.

Mol.	Trans.	E_u/k_B (K)	Frequency (GHz)	Tel./Inst.-band	η_{MB}	Beam size (")	Spec. Resol. (km s^{-1})
C^{18}O	3–2	31.6	329.331	JCMT/APEX	0.63	20 ^b	0.27
	9–8	237.0	987.560	HIFI-4a	0.74	23	0.15 ^a
	10–9	289.7	1097.163	HIFI-4b	0.74	21	0.14 ^a
HCO^+	4–3	42.8	356.734	JCMT/APEX	0.63	14	0.27
	6–5	89.9	535.062	HIFI-1a	0.76	40	0.28

Notes. The beam efficiency for each HIFI band is taken from Roelfsema et al. (2012). The η_{MB} for the JCMT data is retrieved from the Joint Astronomy center website:

http://www.jach.hawaii.edu/JCMT/spectral_line/General/status.html.

(^a) WBS data. (^b) Central spectrum extracted after convolving the map to 20".

the H_2^{18}O $1_{10}-1_{01}$ line for a few low- and high-mass YSOs (Benz et al., in prep.), representing one third of the studied YSOs in this paper.

The $J = 4-3$ lines were observed with the JCMT and APEX telescopes, and retrieved from the LOMASS database⁴ and the Canadian Astronomy Data Centre⁵ for the low- and high-mass YSOs respectively. In general, the observing mode of the HARP instrument, the spectral and spatial resolution of the data, and the procedure to extract and re-bin the HCO^+ $J = 4-3$ data are the same as those used for the C^{18}O $J = 3-2$ data (see Sect. 3.2.2 and Yıldız et al. 2013). The main properties of these two HCO^+ lines can also be found in Table 3.2.

3.2.4. Characteristics of the observed line profiles

As indicated in San José-García et al. (2013), the C^{18}O $J = 3-2$, $9-8$ and $10-9$ lines are considered optically thin and show Gaussian-like profiles. The spectra are characterised by a single narrow ($<7 \text{ km s}^{-1}$) velocity component, attributed to quiescent envelope material. However, for sources with strong outflows, such as G10.47+0.03 and W3-IRS5, additional broad line wings are identified even in the C^{18}O spectra. In order to isolate the contribution from the envelope, the emission from the outflow was subtracted by applying a two Gaussian decomposition method to those sources indicated in Table 3.3 (see San José-García et al. 2013 for details).

On the other hand, both HCO^+ transitions show clear asymmetric profiles for four low-mass protostars and for eight out of nine massive YSOs. The $J = 4-3$ spectra often show both double-peaked and asymmetric line profiles while the $J = 6-5$ transition is only skewed. The asymmetry measured in these lines can be characterised by several parameters such as the ratio of the blue peak intensity and the red peak intensity of the double-peaked profile, T_B/T_R , and the skewness (equation 1 of Gregersen et al. 1997). These parameters are measured for the $J = 4-3$ transition of the studied sources and presented in Table 3.6 of Appendix 3.B. The skewness is negative for 11 sources and the blue/red ratio larger than one for eight YSOs, suggesting the presence of infalling material. As for some C^{18}O spectra, broad line wings are subtracted from both HCO^+ transitions for all sources to exclude the contribution from the outflows.

3.3. Modelling of the observations

The C^{18}O and HCO^+ lines are modelled using the non-LTE radiative transfer code RATRAN (Hogerheijde & van der Tak 2000) assuming spherical symmetry with 1-D density and temper-

⁴<http://lomass.strw.leidenuniv.nl> (in prep.)

⁵<http://www.cadc-ccda.hia-ihh.nrc-cnrc.gc.ca/en/jcmt/>

ature structures. As the observations presented here do not have sufficient spatial resolution to significantly resolve the inner envelope, any additional free parameters required to model C^{18}O and HCO^+ in aspherical geometries would be poorly constrained and would only add degeneracy. The process is composed of two steps, where first the excitation (fractional population) of levels for each cell are computed while the second step uses ray-tracing to create synthetic observations for a given beam.

3.3.1. Source structure

The temperature and density profiles used as inputs for our RATRAN models are taken from Kristensen et al. (2012) for the low-mass and van der Tak et al. (2013) for the high-mass sources. These have been constrained using the continuum radiative transfer codes DUSTY (Ivezić & Elitzur 1997) and a modified version of HOCHUNK3D (Whitney et al. 2013, Robitaille 2011, hereafter WR), respectively. The density structure of the envelope is assumed to follow a power law with index p , i.e., $n \propto r^{-p}$. In the case of low-mass protostars, the outer radius of the envelope was restricted to the smaller radius obtained either when the temperature reaches 10 K or when the density drops below 10^4 cm^{-3} , whichever comes first. For the high-mass YSOs, the envelope is cut at the radius at which the emission of the $450 \mu\text{m}$ SCUBA maps falls below 3σ noise level (see Sect. 4.1 van der Tak et al. 2013). The dust temperature is obtained from continuum radiation transfer calculations for a given luminosity of the source using the Ossenkopf & Henning (1994) dust opacities for grains with thin ice mantles. The gas temperature is assumed to be equal to the dust temperature. The input structures for each YSO are summarised in Table 3.7 in Appendix 3.B. It is important to highlight that the DUSTY and WR models do not realistically reproduce the envelope physical structure on scales of $<100 \text{ AU}$ for the low-mass protostars (see Kristensen et al. (2012), Appendix C) and on scales of $<10^3 \text{ AU}$ for the high-mass YSOs, respectively.

The collisional rate coefficients for the line calculations are taken from the Leiden Atomic and Molecular Database (LAMDA⁶; Schöier et al. 2005, Yang et al. 2010, Flower 1999). We consider collisions with both ortho and para H_2 assuming that the ortho-to-para ratio is thermal with maximum and minimum values of 3 and 10^{-3} respectively (Pagani et al. 2009). The C^{18}O and HCO^+ line profiles are then simulated separately, and convolved to the actual beam of the observations assuming abundance profiles discussed in Sect. 3.3.4. In the following subsections we discuss the fixed and free input parameters, as well as the technique used to determine the best-fit.

We use a grid of 50 cells sampled logarithmically such that each contains equal mass. The dust temperature from the dust continuum models is then interpolated onto this grid for the central radius of each cell.

3.3.2. Non-thermal motions: parameters

San José-García et al. (2013) showed that thermal motions contribute less than 5% to the total observed C^{18}O line width in these objects. Therefore, the C^{18}O and HCO^+ line widths and shapes are dominated by non-thermal motions such as turbulence and infall. In order to quantify the balance of these contributions in protostellar envelopes for a given abundance profile, a grid of models with different values of infall, v_r , and turbulent motions (defined as the Doppler b -parameter, b_t) is consistently run for all sources. The infall velocities are calculated as in Mottram et al. (2013) by assuming that material is in free-fall towards the central forming star, adopting different stellar masses in order to get different infall velocities. The infall velocity of each cell is obtained using the relation: $v \propto r^{-0.5}$. We chose the value at a distance of 1000 AU, $v_{r=1000\text{AU}}$, to characterise the specific infall velocity motion. On the other hand, the turbulent Doppler- b_t component is considered constant as a function of radius and defined in the RATRAN models as $0.6 \times FWHM$ for lines with a gaussian-like profile.

⁶<http://home.strw.leidenuniv.nl/~moldata/>

3.3.3. Fitting method: iteration technique

The procedure to determine the best-fit value of the infall and turbulence motions, v_t and b_t , for each source is based on the assumption that the velocity field must be consistent between HCO^+ and C^{18}O . The optically thick HCO^+ lines are used to restrict the infall component while the optically thin C^{18}O data constrain the turbulent component. The main steps of this procedure are illustrated in the flow-chart shown in Fig. 3.1 and summarised below. Further and more technical details of the method are presented in Sect. 3.B.1 of Appendix 3.B. A ‘‘jump’’ abundance profile with an inner and outer abundance, X_i and X_o respectively, has been assumed for the C^{18}O lines, while for HCO^+ we are using a simpler constant abundance profile, X_o , across the envelope. More details about the determination of these two types of abundance profile are presented in Sect. 3.3.4.

The iteration technique to fit the observations starts by using a trial value for the HCO^+ abundance taken from previous studies (Hogerheijde et al. 1999; Cox et al. 1987; Jørgensen et al. 2004; Godard et al. 2010; Zinchenko et al. 2009; Kim et al. 2006). After improving the value of $X_o[\text{HCO}^+]$ by comparison with an initial test-model, a grid of RATRAN models covering a wide interval of $v_{\text{r}}=1000\text{AU}$ and b_t values (from 0 to $\sim 12\text{ km s}^{-1}$ and from 0 to $\sim 5\text{ km s}^{-1}$ respectively) with steps of $\Delta v_{\text{r}}=0.5\text{ km s}^{-1}$ and $\Delta b_t=0.5\text{ km s}^{-1}$ is run for a fixed value of $X_o[\text{HCO}^+]$. The output images are compared to the HCO^+ observations and the best-fit is obtained via a reduced chi-squared test, χ_{r}^2 , calculation. From this iteration we obtain a first estimation of the infall and turbulent velocities, $v_{\text{r}1}$ and $b_{\text{t}1}$.

Similarly to the HCO^+ data, a trial value for the inner and outer C^{18}O abundance is assumed from previous studies (Jørgensen et al. 2004, Yıldız et al. 2013, Herpin et al. 2012, amongst others) for all sources. These abundance values are refined after running a grid of models in which the estimated $v_{\text{r}1}$ and $b_{\text{t}1}$ are considered fixed parameters and the outer and inner abundance varied in steps of $\Delta X_o[\text{C}^{18}\text{O}]=5\times 10^{-9}$ and $\Delta X_i[\text{C}^{18}\text{O}]=1\times 10^{-8}$ respectively. With the updated C^{18}O abundance profile, a grid of models for C^{18}O is run varying only the turbulent velocity and taking $v_{\text{r}1}$ as a fixed parameters. The output models are compared to the C^{18}O observations, χ_{r}^2 calculated, and the value of b_t updated from the best-fit model. The purpose of this step is to constrain the turbulent component, b_t , with the C^{18}O data.

With the turbulent and infall velocities partially restricted, we refine the value of $X_o[\text{HCO}^+]$ by running a grid of HCO^+ models in which both b_t and v_t are considered fixed parameters and the abundance varies in steps of $\Delta X_o[\text{HCO}^+]=5\times 10^{-10}$. Subsequently, another grid of RATRAN models is run for HCO^+ varying only $v_{\text{r}}=1000\text{AU}$ and taking the new value of $X_o[\text{HCO}^+]$ and the b_t -component as fixed parameter. In this step we constrain the infall velocity by taking the value of $v_{\text{r}}=1000\text{AU}$ from the model that best-fit the observations.

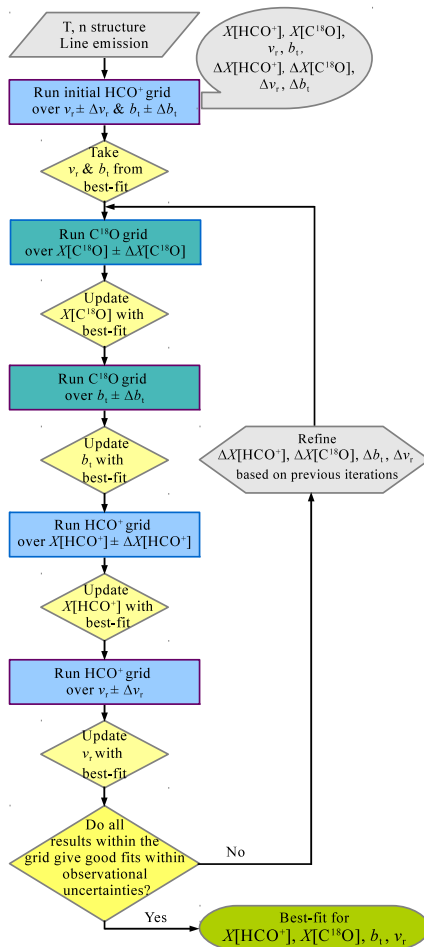


Figure 3.1: Flow-chart diagram with the steps of the iteration technique used to constrain the abundance of HCO^+ and C^{18}O and the infall and turbulent velocities for each source.

As indicated in Fig. 3.1, the entire process is repeated several times reducing the range over which both $v_{r=1000\text{ AU}}$ and b_t are varied and decreasing Δv_r , Δb_t , $\Delta X_o[\text{C}^{18}\text{O}]$, $\Delta X_i[\text{C}^{18}\text{O}]$ and $\Delta X_o[\text{HCO}^+]$ in each iteration until a consistent solution is achieved, i.e., all results from a grid of models fit the observations within their uncertainty. In addition, χ_r^2 values of the C^{18}O modelling are calculated globally, i.e., considering all the available lines, and separately for the low- J (JCMT/APEX data) and the high- J (HIFI $J = 9-8$ and $J = 10-9$) spectra with the purpose of comparing the best solution between different parts of the envelope with the global best-fit.

3.3.4. Abundance profiles

Structure of the abundance profiles

Although the focus of this paper is on the dynamics, the line fitting requires an abundance structure determination. For the C^{18}O lines, a “jump” abundance profile is used, consistent with previous work of Jørgensen et al. (2002) and Yıldız et al. (2012). This profile is characterised by having two different and constant values for the abundance (an inner, X_i , and an outer abundance, X_o) separated at the radius at which the envelope reaches the ice sublimation temperature, T_{eva} . Both $X_i[\text{C}^{18}\text{O}]$ and $X_o[\text{C}^{18}\text{O}]$ are free parameters while T_{eva} is taken as a fixed parameter. On the other hand, a constant abundance profile is chosen for HCO^+ in which a value of the abundance, $X_o[\text{HCO}^+]$, is constant across the envelope.

To justify the selection of a “jump abundance profile” for C^{18}O but not for HCO^+ and to understand which regions of the envelope the observed lines are probing, it is instructive to examine where the bulk of the C^{18}O and HCO^+ emission in each line is generated. Figure 3.2 presents the cumulative intensity in the observed C^{18}O (*middle* panels) and HCO^+ (*bottom* plots) transitions as functions of radius for two example sources, one low-mass (Ser SMM1) and one high-mass (IRAS18089-1732). Their temperature and density profiles as functions of radii are shown in the *top* panels of that figure. The cumulative intensity is calculated from the outside-in by removing successive cells from the model, re-running the ray-tracing and calculating the ratio of the integrated intensity in the new image to the total for all cells considering the whole-envelope, as in Mottram et al. (2013).

For Ser SMM1, 80% of the total emission for the C^{18}O $J = 3-2$ is generated between ~ 200 and 2000 AU. The interval of temperature and density corresponding to this area ranges from 20 to 45 K and $(0.2-3.4)\times 10^7\text{ cm}^{-3}$, respectively. For the high- J lines, 80% of their emission takes place between 60 and 400 AU, characterised by a range of temperature and density varying from 45 to 160 K and $(1.5-25.0)\times 10^7\text{ cm}^{-3}$. Thus, each group of lines probes different parts of the protostellar envelope and there is a small area in which both regimes overlap where less than 30% of the $J = 3-2$ emission originates. Still, it is important to recognise that a large fraction of the high- J emission originates from regions of the envelope with $T < 100$ K (Yıldız et al. 2010). On the other hand, 80% of the emission of both HCO^+ $J = 4-3$ and $J = 6-5$ lines comes from the same region of the envelope (between 200 and 1500–2000 AU), as expected due to the similar E_{up} of the two HCO^+ transitions. This area is characterised by temperatures similar to those where the bulk of emission of the C^{18}O $J = 3-2$ line comes from (see *right* panels of Fig. 3.2).

For IRAS18089-1732, 80% of the C^{18}O emission comes from regions ~ 15 K warmer than those of Ser SMM1, and located one order of magnitude further from the protostar. This is because its envelope is more extended and temperature profiles warmer than for Ser SMM1 (see *top* panels of Fig. 3.2). There is also a region in which the emission of the low- and high- J lines overlap, but in this case the bulk of the emission comes mainly from the high- J lines since the contribution of the $J = 3-2$ transition to the total emission is $< 15\%$. Looking at the cumulative intensity of the HCO^+ lines for this source (*bottom-right* panel of Fig. 3.2), 80% of the total HCO^+ emission is generated in a more extended area (from 10^3 to 10^4 AU) with warmer temperatures (40–200 K) compared to the HCO^+ emission of Ser SMM1. For both low- and high-mass YSOs we measure an increase in intensity for the $J = 4-3$ line after removing the cells of the outer parts of the envelope, mostly due to absorption of emission by these colder outer layers of the envelope.

Therefore, the studied C^{18}O line are probing different areas of the envelope with different

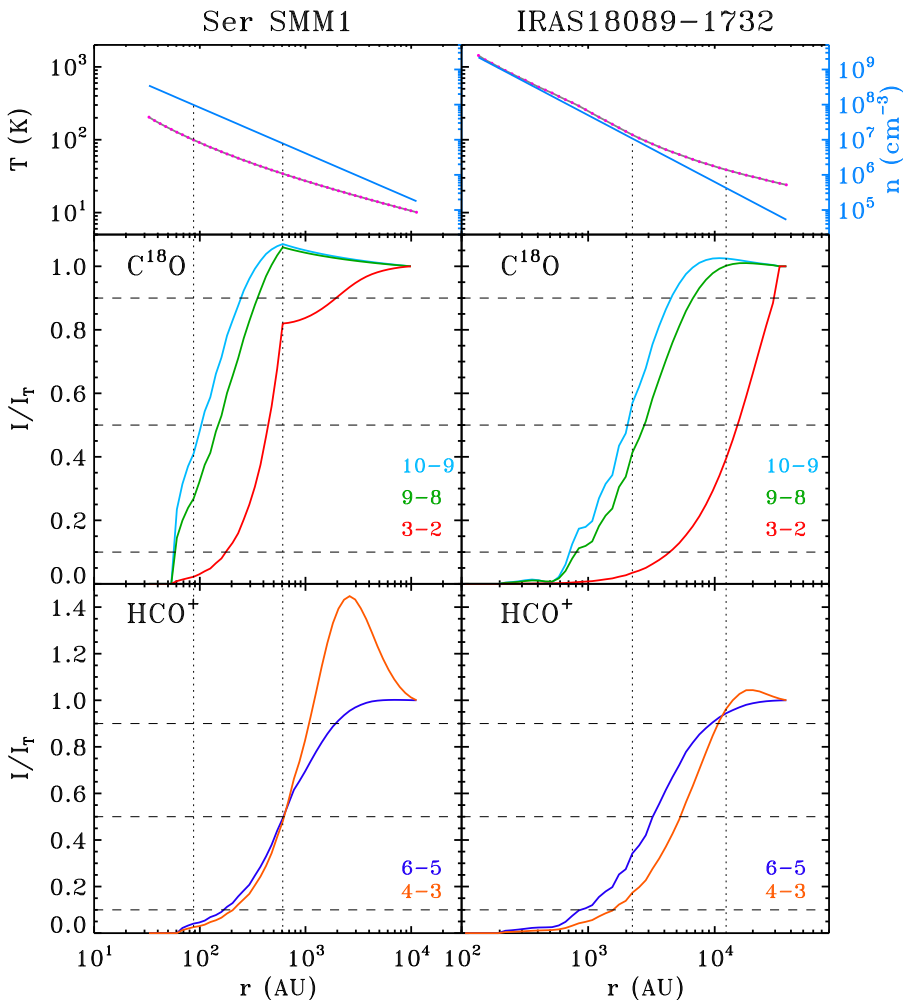


Figure 3.2: The *top* panels show the temperature (dark grey) and density profiles (blue) of the low-mass Class 0 Ser SMM1 (*left* column) and the high-mass YSO IRAS18089-1732 (*right* column) as a function of radius. The pink points indicate the temperature value for each RATRAN cell interpolated from the dust models. The *middle* panels corresponds to the cumulative contribution of material inside a given radius to the total intensity of the C^{18}O $J=3-2$ (red), $J=9-8$ (green) and $J=10-9$ (blue) lines for the same low- and high-mass objects. Similarly, the *bottom* figures show the cumulative contribution for the HCO^+ $J=4-3$ (orange) and $J=6-5$ (dark blue) lines of those sources. The dashed lines in the *middle* and *bottom* plots indicate the levels corresponding to 10, 50 and 90%. The vertical dotted lines mark the radii at which the gas and dust temperature reaches 100 and 35 K respectively.

conditions, thus a “jump” abundance profile can be constrained with the available data. The two HCO^+ observations come from approximately the same region, so a drop in abundance at a certain radius cannot be constrained and would only add larger uncertainties to the results. The “jump” abundance profile is used also for the massive object NGC6334-I(N), the only source for which the C^{18}O $J=3-2$ spectrum is not available. The assumed value of its outer abundance is the average of the $X_{\text{O}}[\text{C}^{18}\text{O}]$ values obtained for the other massive objects. Its precise choice does not affect the results.

Our modelling shows that a jump in the C^{18}O abundance is required to fit all C^{18}O transitions for both low- and high-mass YSOs (see Fig. 3.3 as illustration for one source). In the case of the

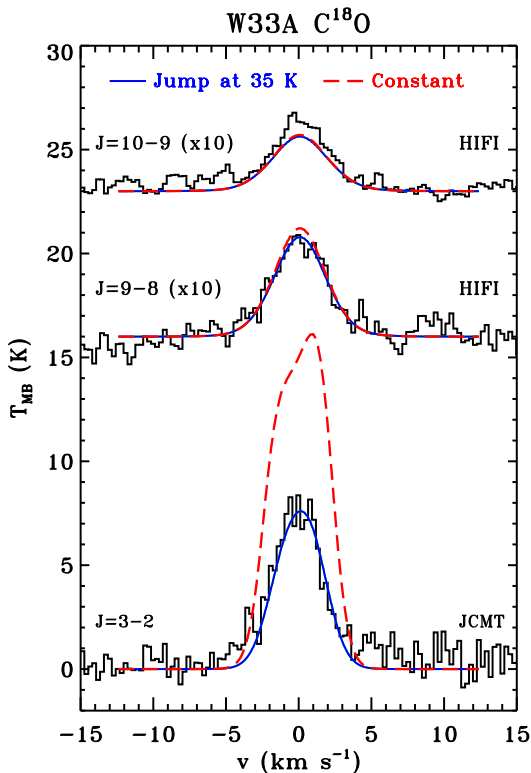


Figure 3.3: Comparison between the “jump abundance” (solid blue lines) and the constant abundance (dashed red lines) profiles for the C^{18}O observations of the high-mass YSO W33A. The value of the C^{18}O abundance for the red model is 4.0×10^{-7} . In the case of the blue output images, the inner abundance, $X_i[\text{C}^{18}\text{O}]$, is also 4.0×10^{-7} , the outer abundance, $X_o[\text{C}^{18}\text{O}]$, is 2.0×10^{-8} and the evaporation temperature is 35 K.

low-mass protostars, models in which the evaporation temperature is lower than 30 K result in too much emission in the C^{18}O $J = 3-2$ line and those with T_{eva} larger than 45 K underproduce the intensity of the high- J lines by more than 20%. A similar situation is observed for the high-mass objects with the difference that for several high-mass objects, a T_{eva} lower than 30 K cannot be tested because the temperature never drops below 30 K at the outer edge of their envelopes. Since a jump is needed to reproduce the observations for all sources (see Fig. 3.3), T_{eva} must be higher than 30 K.

Therefore, we adopt a T_{eva} for C^{18}O of 35 K for the entire sample of YSOs because it is the lowest temperature for which the RATRAN models reproduce the line intensity of the three studied C^{18}O transitions in both low- and high-mass objects. The chosen value of T_{eva} is higher than laboratory measurements for pure CO ices (Collings et al. 2004; Öberg et al. 2005; Bisschop et al. 2006), but possible for mixed ices with species such as CO_2 . A similar value of T_{eva} of 35 K was previously inferred for some low-mass objects by Jørgensen et al. (2005).

Inferred abundances

The values of the abundance profile derived for C^{18}O and HCO^+ from the best-fit models are summarised in Table 3.3. The estimated uncertainties for the C^{18}O and HCO^+ abundances are less than a factor of two. In addition, Table 3.4 summarises the mean of the inner and outer C^{18}O abundances, of the ^{12}CO abundance derived from those results, and of the constant HCO^+ abundances. These values are computed separately for the low- and high-mass sub-samples, and for the entire sample of YSOs.

In general all sources have similar $X_i[\text{C}^{18}\text{O}]$ values within the uncertainty of the models. On the other hand, the outer C^{18}O abundance profile varies from 2.0×10^{-9} to 4.0×10^{-7} within the low- and high-mass sub-samples. $X_o[\text{C}^{18}\text{O}]$ shows the largest interval of variation either because

Table 3.3: Best-fit value of the $C^{18}O$ inner and outer abundance, expected maximum $C^{18}O$ abundance, and ^{12}CO abundance derived from the best-fit value of the inner $C^{18}O$ abundance of each source. The value of the HCO^+ abundance for the best-fit RATRAN models are also indicated.

Source	$X_o[C^{18}O]$	$X_i[C^{18}O]$	$X_{MAX}[C^{18}O]^a$	$X_i[^{12}CO]^b$	$X_o[HCO^+]$
Low-mass					
NGC1333 IRAS 2A ^e	3.0(-8)	1.5(-7)	4.9(-7)	8.2(-5)	1.0(-9)
NGC1333 IRAS 4B ^e	1.5(-8)	3.5(-7)	4.9(-7)	1.9(-4)	5.0(-10)
Ser SMM1 ^e	7.0(-9)	4.9(-7)	5.1(-7)	2.6(-4)	6.0(-10)
GSS30 IRS1	2.5(-7)	5.5(-7)	5.1(-7)	2.9(-4)	1.0(-9)
Elias 29	4.0(-7)	1.9(-6)	5.1(-7)	1.0(-3)	3.0(-9)
High-mass					
IRAS05358+3543	2.0(-9)	3.1(-7)	4.2(-7)	2.0(-4)	6.0(-10)
NGC6334-I(N) ^{d,e}	1.0(-7)	6.0(-7)	6.2(-7)	2.6(-4)	3.0(-10)
DR21(OH)	5.0(-9)	5.0(-7)	5.1(-7)	2.7(-4)	8.0(-10)
W3-IRS5 ^{c,e}	1.0(-7)	8.3(-7)	4.3(-7)	5.1(-4)	1.3(-9)
IRAS18089-1732	2.0(-7)	2.8(-7)	6.7(-7)	1.1(-4)	8.0(-10)
W33A	2.0(-8)	4.0(-7)	6.7(-7)	1.6(-4)	3.2(-10)
IRAS18151-1208	2.0(-7)	6.3(-7)	7.2(-7)	2.4(-4)	2.5(-10)
G10.47+0.03 ^c	3.5(-7)	5.0(-7)	1.2(-6)	1.1(-4)	1.0(-9)
G34.26+0.15	2.0(-7)	4.2(-7)	6.9(-7)	1.7(-4)	9.0(-10)

Notes. (a) Maximum $C^{18}O$ abundance obtained from the expected $^{16}O/^{18}O$ isotopic ratio (Table 3.1) and assuming a CO/H_2 ratio of 2.7×10^{-4} (Lacy et al. 1994). (b) ^{12}CO abundance derived from $X_i[C^{18}O]$ and the expected $^{16}O/^{18}O$ isotopic ratio. (c) Sources for which line wings were removed for the $C^{18}O$ spectra. (d) The $C^{18}O J = 3-2$ line is not available for this source. (e) $HCO^+ J = 6-5$ line was observed.

Table 3.4: Mean values of the $C^{18}O$ abundance translated to ^{12}CO according to the $^{16}O/^{18}O$ isotopic ratio presented in Table 3.1.

Sample	$\bar{X}_o[C^{18}O]$ ($\times 10^{-7}$)	$\bar{X}_i[C^{18}O]$ ($\times 10^{-7}$)	$\bar{X}_o[^{12}CO]$ ($\times 10^{-5}$)	$\bar{X}_i[^{12}CO]$ ($\times 10^{-4}$)	$\bar{X}_o[HCO^+]$ ($\times 10^{-10}$)
Low-Mass ^a	0.8 ± 0.5	3.9 ± 0.8	4.0 ± 3.0	2.1 ± 0.4	7.8 ± 1.1
High-Mass	1.6 ± 0.4	5.0 ± 0.5	6.4 ± 1.8	2.2 ± 0.4	9.3 ± 1.9
Total	1.3 ± 0.3	4.6 ± 0.4	5.7 ± 1.5	2.2 ± 0.3	8.8 ± 1.8

Notes. (a) The mean and uncertainty have been calculated without including Elias 29 (see Appendix 3.A.1).

we have only one line available to confine this parameter at those radii or because the intrinsic properties of these regions are different from source to source. As for $X_i[C^{18}O]$, the values of the best-fit HCO^+ abundance are comparable from low- to high-mass and to the mean (8.8×10^{-10}).

The best-fit values of the $C^{18}O$ abundance are compared to the expected maximum $C^{18}O$ abundance, $X_{MAX}[C^{18}O]$, for each YSO. This parameter is computed assuming $[CO/H_2] = 2.7 \times 10^{-4}$, as found for warm dense gas by Lacy et al. (1994), and using the $^{16}O/^{18}O$ isotopic ratio presented in Table 3.1 which were calculated with the relation found by Wilson & Rood (1994). The same expected isotopic ratio is also used to derive the inner ^{12}CO abundance, $X_i[^{12}CO]$, from the best-fit $X_i[C^{18}O]$ parameter. Both $X_{MAX}[C^{18}O]$ and $X_i[^{12}CO]$ are presented in Table 3.3. It is seen that the obtained $X_i[^{12}CO]$ is generally below or of the order of the maximum $[CO/H_2]$ abundance from Lacy et al. (1994) (i.e., all volatile carbon locked up in CO) but significant exceeds it for two sources: Elias 29 and W3-IRS5. Possible reasons explaining the high inner abundance value derived for these two YSOs are discussed in more detail in Appendix 3.A.1 and 3.A.2, respectively.

Finally, the RATRAN models consistently underestimate the $HCO^+ J = 6-5$ emission but reproduce the 4-3 line, even if high HCO^+ abundances are used or a jump in abundance is applied. As the emission in these lines is generated in a similar region, the missing $J = 6-5$ emission is most

likely produced by physical mechanisms not included in our 1-D spherically symmetric models. A possible explanation is that the excess $J = 6-5$ emission comes from the dense outflow cavity walls where the quiescent envelope gas is directly heated by radiation from the central source. This extra emission does not come from any possible disk because the $J = 6-5$ spectra are observed with a $40''$ beam, so the emission would be too beam diluted to be detected. The HCO^+ $J = 6-5$ spectra are further studied and analysed in Benz et al. (in prep.).

3.4. Results

We summarise the results from the RATRAN models focusing on the dynamical structure of the envelope. In Sect. 3.4.1 we first introduce two extreme scenarios in which infall and turbulent velocities adopt different values according to specific assumptions. Then, the values of the velocity field that best fits the C^{18}O and HCO^+ observations simultaneously are analysed and trends with luminosity investigated. Finally, in Sect. 3.4.2 we consider models in which the turbulent component varies with radius and compare to those with constant turbulence across the protostellar envelope.

3.4.1. Velocity field study within the sample

To justify the need for both infall and turbulent motions, we start the study of the dynamical structure of protostellar envelopes by exploring two extreme frameworks: the pure infall-dominated ($b_t=0 \text{ km s}^{-1}$) and the pure turbulent-dominated ($v_r=0 \text{ km s}^{-1}$) scenarios. To illustrate these two types of models, Fig. 3.4 shows the C^{18}O and HCO^+ spectra of the low-mass protostar NGC1333 IRAS2A plotted with the RATRAN model for zero turbulent motions (red solid lines) and for zero infall (blue dashed lines). The corresponding values of the infall and turbulent velocities are $v_r=1.3 \text{ km s}^{-1}$ and $b_t=1.0 \text{ km s}^{-1}$, respectively. These were derived by running a small χ^2 grid with the other velocity component set to zero.

The pure infall-dominated scenario presented in Fig. 3.4 shows a flattening at the peak position of the C^{18}O line profile. Furthermore, additional line wings appear for the higher- J transitions, producing a worse fit to the data. The only features that are well reproduced by the zero-turbulence models are the line wings of the C^{18}O $J = 3-2$ lines, which explains why these models are sometimes selected by the reduced χ^2 calculations as the best fit for this transition. However, when accounting for the global χ_r^2 , calculated as explained in Appendix 3.B.1, models with no contribution from turbulence fall far out of the 1-sigma uncertainty for all our sources.

Similarly to what is seen for C^{18}O in NGC1333 IRAS2A, the shape of the output line profiles and that of the HCO^+ observations do not match when $b_t=0 \text{ km s}^{-1}$. Therefore, we can state that a turbulent component is needed to reproduce these obser-

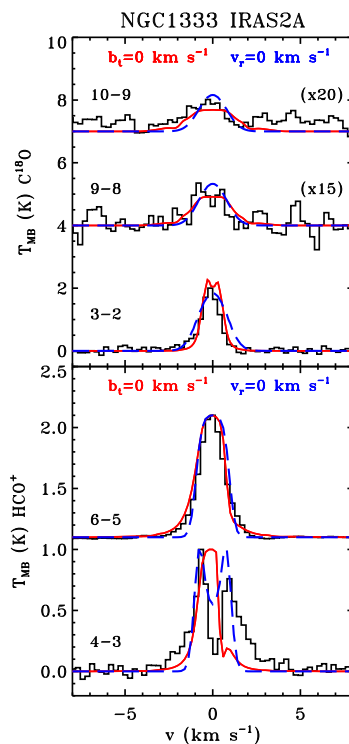


Figure 3.4: (Top) C^{18}O observations of NGC1333 IRAS2A plotted with the derived RATRAN output models. (Bottom) Same as top panel but for the normalised HCO^+ data and models. The turbulent dominated models ($v_r=0.0 \text{ km s}^{-1}$) are shown with dashed blue lines and the infall dominated models ($b_t=0.0 \text{ km s}^{-1}$) with solid red lines.

vations independent of the source luminosity. In addition, if no turbulent motions are added to the models, too high infall velocities are needed to reproduce the broadening of the line profile (generally a factor of 1.5 times the maximum infall velocity according to their estimated masses), as is shown for the high-mass YSO G34.26+0.15 in Fig. 3.15 of Appendix 3.B. These values of v_r imply unreasonably high stellar masses (more than twice the estimated or assumed value). Moreover, the opacity of the lines generated by these models are a factor of two lower than those obtained from models with a turbulent component included, and the HCO^+ lines can even become optically thin, which seems unlikely.

The pure turbulent-dominated scenario ($v_r = 0 \text{ km s}^{-1}$) can properly reproduce the optically thin C^{18}O observations, as is shown in blue in the *top* panel of Fig. 3.4. Therefore, this model could be used to fit optically thin C^{18}O lines, as previously found by Jørgensen et al. (2004), Yıldız et al. (2012). However, if we combine the analysis of the C^{18}O data with the optically thick HCO^+ observations, we can rule out this scenario for all those sources with a skewed or asymmetric double-peak profile (these parameters are calculated for the HCO^+ $J = 4-3$ observations and presented in Table 3.6). In particular, the pure turbulent-dominated models can be discarded for four low-mass protostars and for eight out of nine high-mass YSOs within 1-sigma confidence level (see Fig. 3.4 for the case of IRAS2A).

Therefore, for the assumed envelope structure, we prove that the RATRAN models need to include both a turbulent and an infall component in order to reproduce both C^{18}O and HCO^+ observations simultaneously for $\sim 75\%$ of the YSOs in our sample.

The best-fit values of the infall velocity at a radius of 1000 AU (v_r), turbulence parameter b_t and χ_r^2 results are presented in Table 3.5. The turbulent component is calculated separately for three groups of C^{18}O lines: the low- J transition, the HIFI spectra and the entire set of available observations. The estimated uncertainties for the turbulence and infall velocity are of the order of 0.2 km s^{-1} . In addition, the maximum infall velocity, $v_{r\text{MAX}}$, derived from the estimated stellar mass of the forming star (M_* ; see Table 3.1) is included in this table together with the central gravitational mass, M_g , and the instantaneous mass infall rate, \dot{M}_{inf} . The gravitational mass and mass infall rate are calculated for each source using:

$$M_g = 0.56 \left(\frac{v_{r=1000\text{AU}}}{1 \text{ km s}^{-1}} \right)^2 M_\odot, \quad (3.1)$$

and:

$$\dot{M}_{\text{inf}} = 2.08 \times 10^{-2} \left(\frac{n_0}{10^9 \text{ cm}^{-3}} \right) \left(\frac{v_{r=1000\text{AU}}}{1 \text{ km s}^{-1}} \right) \left(\frac{r_{\text{mdi}}}{r_0} \right)^{-p} M_\odot \text{ yr}^{-1} \quad (3.2)$$

respectively, and assuming that the velocity at 1000 AU, $v_{r=1000\text{AU}}$, obtained from the best-fit RATRAN model is the velocity corresponding to the minimum detectable infall radius, r_{mdi} . M_g ranges from 0.02 to $0.36 M_\odot$ and \dot{M}_{inf} from 1.7×10^{-6} to $9.5 \times 10^{-5} M_\odot \text{ yr}^{-1}$ for the low-mass protostars. These parameters vary from 0.14 to $49.5 M_\odot$ and from 5.4×10^{-4} to $7.6 \times 10^{-3} M_\odot \text{ yr}^{-1}$ for the massive YSOs. Equations 3.1 and 3.2 are as in Mottram et al. (2013) with the exception that a unit conversion error in the latter equation by those authors has been corrected.

The three best-fit RATRAN solutions (for the low- J in green, the high- J in blue and the global in red) are compared with the C^{18}O observations in Appendix 3.A (Figs. 3.8 and 3.9 for the low-mass sample and from Fig. 3.12 to 3.13 for the high-mass YSOs). Similarly, the best-fit RATRAN models for the HCO^+ data normalised to their peak intensities are plotted together with the normalised HCO^+ observations for the low-mass protostars in Figs. 3.10 and 3.11 and for the high-mass objects in Fig. 3.14. The best-fit models generally reproduce the C^{18}O observations in terms of shape and intensity. In the case of the HCO^+ spectra, the profiles of the RATRAN models display similar values of skewness and T_B/T_R ratio as those calculated from the $J = 4-3$ line (see Table 3.6).

Table 3.5: Value of the turbulent, b_t , and infall, v_r , components of the best-fit `RATRAN` model for each YSOs calculated considering all available $C^{18}O$ and HCO^+ observations, respectively. The χ_r^2 of each model is indicated. In addition, the best-fit b_t -parameter is determined considering only the $C^{18}O$ $J=3-2$ transition and the HIFI ($J=9-8 + 10-9$) observations. The gravitational mass derived from the best-fit infall velocity, the instantaneous mass infall rate and the virial turbulent velocity are calculated for those sources with negative infall velocities.

	$J=3-2$		$J=9-8 + 10-9$		Global			v_{rMAX}^a ($km\ s^{-1}$)	M_g^b M_\odot	\dot{M}_{infall}^c $M_\odot\ yr^{-1}$	$b_{ff=1}^d$ ($km\ s^{-1}$)
	b_t ($km\ s^{-1}$)	χ_r^2	b_t ($km\ s^{-1}$)	χ_r^2	b_t ($km\ s^{-1}$)	v_r	χ_r^2				
Low-mass											
NGC1333 IRAS 2A	0.8	4.3	1.5	1.8	1.0	-0.2	4.6	-1.3	0.02	7.1(-6)	0.3
NGC1333 IRAS 4B	0.6	1.7	0.6	0.9	0.6	-0.8	3.9	-1.3	0.36	9.3(-5)	0.5
SerSMM1	0.8	3.7	1.1	1.7	0.8	-0.8	5.3	-1.3	0.36	6.9(-5)	0.7
GSS30 IRS1	0.6	5.6	1.3	1.2	0.6	-0.5	3.5	-1.3	0.14	1.7(-6)	0.1
Elias 29	1.1	5.0	2.4	3.1	1.1	0.5	2.5	-1.3	0.14	-	-
High-mass											
IRAS05358+3543	1.2	1.6	1.9	1.1	1.2	2.2	1.4	-4.4	2.71	-	
NGC6334-I(N)	-	-	-	-	1.9	-0.5	8.5	-3.6	0.14	6.5(-4)	5.1
DR21(OH)	-	-	-	-	2.3	-3.6	6.7	-4.8	7.26	1.3(-3)	2.2
W3-IRS5	-	-	-	-	2.0	-5.1	12.1	-7.9	14.57	5.4(-4)	1.4
IRAS18089-1732	1.9	26.5	2.2	1.4	1.9	-1.9	9.8	-4.9	2.02	2.0(-3)	1.5
W33A	1.4	3.8	1.6	2.3	1.6	4.8	3.0	-6.0	12.90	-	-
IRAS18151-1208	1.1	3.9	1.6	1.9	1.3	-0.8	2.6	-5.2	0.36	1.1(-3)	1.3
G10.47+0.03	2.8	16.4	3.2	1.7	3.0	-9.4	7.1	-9.4	49.48	7.6(-3)	3.2
G34.26+0.15	1.8	23.4	2.3	2.3	2.3	-9.1	19.5	-9.1	46.37	6.7(-3)	3.3

Notes. The values of the infall velocity, v_r , are given at 1000 AU radius.

(*a*) Maximum infall velocity, v_{rMAX} , is calculated from the assumed stellar masses. (*b*) The central gravitational mass, M_g , is derived from the best-fit value of the infall velocity v_r using equation 3.1. (*c*) Mass infall rate derived from the best-fit value of v_r at a radius of 1000 AU is calculated using equation 3.2. (*d*) Virial velocity $b_{ff=1}$ calculated using equations 3.3 and 3.4, assuming that the sources are in virial equilibrium, i.e., $\alpha_{vir} = 1$, and taking R as the outer radius of the envelope (r_{out} , see Table 3.7).

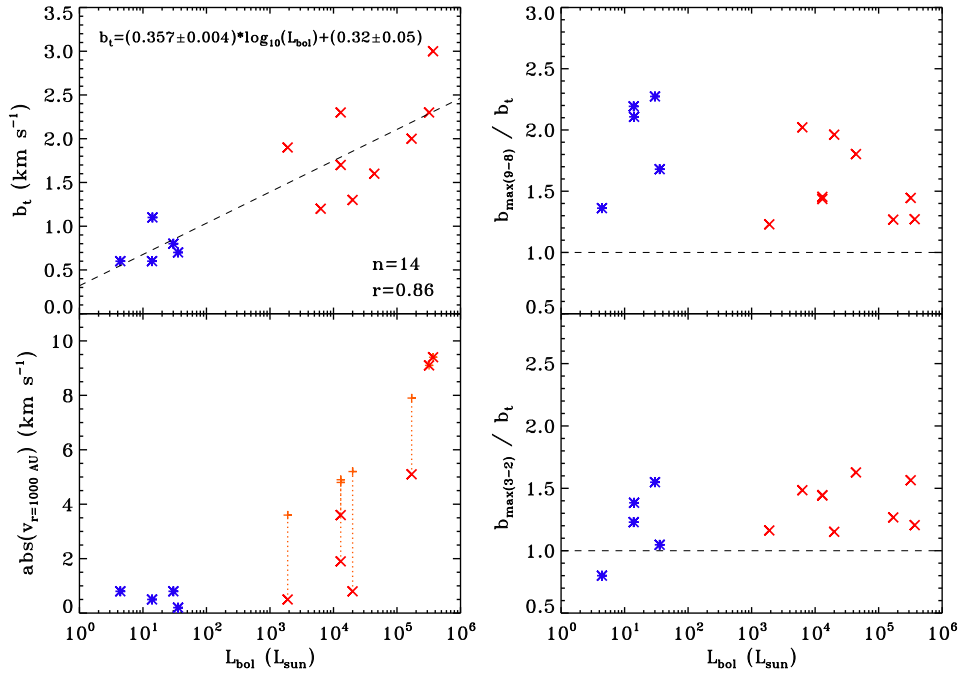


Figure 3.5: (*Top-left*) Best-fit values of the turbulent velocity, b_t , obtained from the `RATRAN` models for each source versus its bolometric luminosity, L_{bol} . The number of sources, n , and the Pearson correlation coefficient, r , are indicated together with the parameters and uncertainties of the linear fit. (*Bottom-left*) Absolute infall velocity value at 1000 AU, $v_{r=1000\text{AU}}$, calculated from the best fit `RATRAN` models versus the source L_{bol} . The blue asterisks correspond to the low-mass objects and the red crosses to the high-mass YSOs. The light orange pluses correspond to the maximum infall velocity at 1000 AU, $v_{\text{MAX}r=1000\text{AU}}$, calculated from the estimated stellar masses indicated in Table 3.1 for the high-mass objects. The values of $v_{r=1000\text{AU}}$ and $v_{\text{MAX}r=1000\text{AU}}$ for each massive YSO are connected with light orange dashed lines.

(*Top-right*) Ratio of the maximum turbulent velocity calculated from the FWHM of the $\text{C}^{18}\text{O } J = 9-8$, $b_{\text{max}(9-8)}$, divided by the best-fit value of the turbulent component, b_t , obtained from the `RATRAN` models for each source versus its L_{bol} . (*Bottom-right*) Same as *top* panel but the maximum turbulent velocity is calculated from the FWHM of the $\text{C}^{18}\text{O } J = 3-2$, $b_{\text{max}(3-2)}$. The blue asterisks correspond to the low-mass protostars and the red crosses to the high-mass YSOs. The dashed black line denotes a ratio of unity.

Turbulent component

To visualise the results of the best-fit parameters (Table 3.5), the left column of Fig. 3.5 presents the global best-fit values of the turbulent velocity, b_t , and the absolute infall velocity at 1000 AU, $v_{r=1000\text{AU}}$, as a function of bolometric luminosity (*top* and *bottom* panels respectively).

Although the dispersion of the data points is significant, the turbulence b_t seems to increase with the logarithm of L_{bol} . This trend is confirmed by a Pearson correlation coefficient, r , of 0.86 and it follows the equation: $b_t = m \log(L_{\text{bol}}) + n$, where $m = 0.357 \pm 0.004$ and $n = 0.32 \pm 0.05 \text{ km s}^{-1}$. In general, for the low-mass protostars, the best-fit for b_t ranges from 0.6 to 1.1 km s^{-1} , while for the high-mass sub-sample b_t is always larger than 1.2 km s^{-1} . Therefore, these results suggest that more massive objects are characterised with larger turbulent velocities, as seen previously in e.g. Marseille et al. (2010); Herpin et al. (2012). This result is further discussed in Sect. 3.5.1. In addition, this increase with luminosity is consistent with the broadening of the intrinsic line width of the C^{18}O observations with L_{bol} observed by San José-García et al. (2013).

The maximum turbulent velocity, b_{max} , for each source can be calculated from the line width of the observed C^{18}O lines ($b_{\text{max}} = 0.6 \times \text{FWHM}$, see Sect. 3.3.2, where FWHM has been quantified by fitting the observations with a Gaussian profile), by assuming that only turbulent motions

broaden the line. The spectra from different C^{18}O transitions give the maximum value of Doppler- b at different radii since the bulk of their emission is generated in different regions of the envelope (Fig. 3.2). The right column of Fig. 3.5 shows the ratio of b_{max} calculated from the FWHM of the C^{18}O $J = 9-8$ lines (*top-right*) and the b_{max} derived from the FWHM of the $J = 3-2$ spectra (*bottom-right*) divided by the b_t parameter of the best-fit RATRAN models for each source as a function of L_{bol} .

For the low-mass protostars, that ratio increases from 0.8–1.6 to 1.4–2.3 from the $J = 3-2$ to the $J = 9-8$ line. According to our envelope model, this increase indicates that turbulence mainly causes the broadening of the line width for low- J transitions, i.e., in the outer colder parts of the envelope. However, in the inner warmer regions traced by higher- J lines, infall motions might create the extra emission which broadens the C^{18}O $J = 9-8$ with respect the $J = 3-2$ as turbulence alone cannot explain the increase of the line width. Then, we confirm that not only is infall needed to reproduce the C^{18}O and HCO^+ observations simultaneously, but it is also a plausible mechanism capable of explaining the significant increase in the line-width from low- to high- J transitions for this sub-sample of YSOs (see also Harsono et al. 2013).

For the high-mass objects, the value of b_t from the best-fit models is lower than b_{max} for both lines, so again, the observed line width cannot be explained by turbulent motions alone. The increase of the line width at high- J transitions is not as evident as for the low-mass protostars, which suggests that the effect of turbulent and infall motions on the C^{18}O line profiles is similar across the regions of the envelope probed by those transitions. However, the emission from infalling material might become slightly more important in the inner regions traced by the high- J spectra than in those traced by lower- J lines since the velocity increases towards smaller radii, likely causing the extra broadening of those profiles.

Infall component

The maximum infall velocity at a radius of 1000 AU ($v_{r,\text{MAX}}$; see Table 3.5) for each source is plotted in Fig. 3.5 (*bottom-left*) with lighter colours and plus symbols. For low- and high-mass YSOs, the best-fit value of v_r is always lower or comparable to the assumed and estimated maximum infall velocity. Two different regimes corresponding to the two sub-samples of objects are seen. In the case of the low-mass protostars, the best-fit for v_r remains always below 1 km s^{-1} , independently of the luminosity of the source. For the high-mass objects, an increase in the infall velocity at higher luminosities is observed. The interval of possible solutions within 1 sigma confidence level for v_r is narrower for the low-mass protostars than for the massive YSOs because b_t is smaller as well.

Many of the high-mass YSOs have infall velocities below that expected for free-fall. A possible reason is that M_* in Table 3.1 is calculated assuming that a single main-sequence star is responsible for the total luminosity, when accretion may also contribute, depending on the mass infall rate and accretion radius. Another explanation is that material may infall slower than the free-fall velocity due to strong turbulent mixing, counter-flows along the outflow cavity wall or drag from coupling to magnetic fields.

For two high-mass YSOs, IRAS05358+3543 and W33A, a positive v_r component is required to reproduce the HCO^+ $J = 4-3$ spectrum, meaning that the bulk of gas traced by these observations on the relevant scales (10^3 – 10^4 AU) is mainly in expansion rather than infalling. Constraining this expansion would require an extra free parameter which would be hard to constrain with only two HCO^+ transitions that probe the same material. To be consistent with the assumed physical structure of the envelope and adopted velocity field of the models, these sources are considered as outliers in our analysis and are not included in the *bottom-left* panel of Fig. 3.5 to avoid confusion in the interpretation of this result. Other molecular line observations have shown indications of both infall and expanding motions, see van der Tak et al. (2013).

Fig. 3.6 presents the contribution of infall motion to the total velocity field in the best-fit model of both C^{18}O and HCO^+ as a function of the fractional radius for the low- (*left*) and high-mass (*right*) YSOs. As seen in the figure, the radius at which less than 50% of the total emission is caused by infalling material is different for each YSO and its contribution falls rapidly with increasing

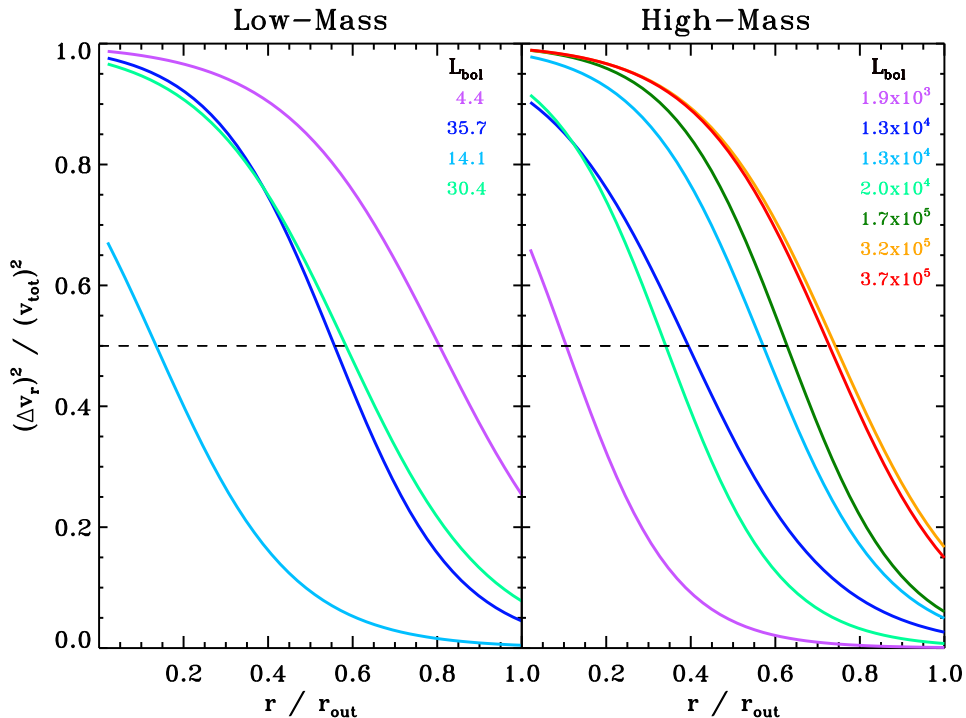


Figure 3.6: Percentage of the contributed infall (solid lines) broadening to the total modelled line width v_{tot} for the obtained best-fit model as a function of the fractional radius of the modelled envelope for the low- (*left* panel) and high-mass (*right* panel) YSOs. The bolometric luminosity of each source, indicated in the right-up corner of each panel, are given in units of solar luminosity. The 50% contribution to the total line width is indicated with an horizontal dashed black line.

radii. Within the high-mass sub-sample, for objects with luminosities up to $2.4 \times 10^4 L_{\odot}$, infall dominates in their inner half of the envelope, corresponding to the radii less than a few 1000 AU, with the importance of infall increasing with luminosity, i.e., stellar mass. Since most of the emission in low- and high- J C^{18}O and HCO^+ transitions originates at larger radii (e.g. see right column panels of Fig. 3.2), this result implies that our lines are turbulence dominated and these motions cause more than 50% of the line broadening.

In the case of the low-mass protostars, this systematic behaviour cannot be confirmed because the number of sources is small. However, the left panel of Fig. 3.6 shows that for three out of four protostars the infall component causes a substantial contribution to the line width until 60–80% the modelled envelope (1000 AU), indicating that both mechanisms are important. Only for IRAS2A (light blue) does turbulence dominate over most of the envelope.

3.4.2. Models with radius-dependent turbulence

In order to explain the observed increase of the C^{18}O line width at higher- J transitions for the low-mass protostars, we test a model in which b_t decreases smoothly at larger radii instead of remaining constant across the envelope. This scenario implies an increase in turbulent motions in the inner warmer regions of the envelope, consistent with the idea of outflows or winds from the forming star injecting turbulence into the inner envelope. The structure is tested on the C^{18}O observations of Ser SMM1 assuming free-fall and taking $v_{r=1000\text{AU}}$ as -0.8 km s^{-1} from the best-fit model. Then, the linear profile describing the decrease of the turbulent motions with radii fol-

lows the equation: $b_t = m \times \log_{10}(R) + n$, with $m = (b_{tJ=9,10} - b_{tJ=3}) / (R_{J=9,10} - R_{J=3}) = -0.8$ and $n = b_{tJ=9,10} - m \times \log_{10}(R_{J=9,10}) = 12$. $R_{J=9,10}$ and $R_{J=3}$ correspond to the central radii at which 80% of the high- and low- J $C^{18}O$ lines are generated (see Fig. 3.2, *left* panels) while $b_{tJ=9,10}$ and $b_{tJ=3}$ are the best-fit solutions of the turbulent component for each sub-group of lines computed from the RATRAN models.

Figure 3.16 presents the output spectra for this model plotted in red on top of the observations, as well as the best-fit using a constant turbulent line-width for just the low and high J lines shown in green ($b_t = 0.8 \text{ km s}^{-1}$) and blue ($b_t = 1.6 \text{ km s}^{-1}$), respectively. The model in which the turbulence varies as a function of radius fits the width of the observations at all J . However, the line profiles in the gradient model have a triangular shape which differs from the characteristic Gaussian-like shape observed in the $C^{18}O$ observations. This triangular profile is more prominent in the lower- J transition than in the HIFI lines. The line-profiles produced by this turbulence gradient model do not agree with the observations, especially at the center of the line. Since the fit actually gets worse (χ_r^2 also increases), we keep the original model with constant turbulent velocity across the envelope.

Similarly, we test the scenario in which turbulence increases linearly as a function of radius. This positive gradient in turbulence agrees with the expected dynamical structure of massive protostellar envelopes, with inner regions showing a lower degree of turbulence because the high densities of those areas dissipate those motions. However, these models result in $C^{18}O$ line profiles with slightly broader width for the lower- J transitions that do not reproduce the observations for the high-mass YSOs, for which the line widths remain practically constant or even seem to slightly increase for the high- J transitions. Figure 3.17 shows the output profiles of two models with a positive gradient in turbulence (green and blue profiles) run for the high-mass object IRAS18089-1732 and our best-fit model in which b_t remains constant as a function of radius (red profiles). The turbulent gradient in the model of the blue profile is steeper than that of the green profile. It is seen that a model with constant turbulent velocity reproduces better low- and high- J transitions simultaneously and adds less degeneracies to the solutions. Once again we preserve the original model because it produces the best fit for both low- and high-mass objects, especially for the higher- J $C^{18}O$ transitions.

Other RATRAN models with varying turbulent velocity across the envelope have been used to reproduce both CO and water observations. An example is presented in Herpin et al. (2012). In this work, the authors modelled 14 HIFI water lines of the massive YSO W43-MM1 assuming a “multiple-step” velocity field. For this profile, the turbulent component and absolute value of the infall velocity increase with radius at steps located at specific values of envelope temperature. The Herpin et al. (2012) model for H_2O was run for the $C^{18}O$ lines of W43-MM1 in order to test if it can reproduce all observed $C^{18}O$ transitions simultaneously. Figure 3.18 shows in red the output RATRAN models of the “multiple-step” velocity profile and in blue the solutions from the model with constant turbulent velocity across the envelope and free fall motions. The former results in profiles with broader line widths for the lower- J transitions, which is not consistent with the observations. In addition, the peak of the modelled $C^{18}O$ lines are too blue-shifted. On the other hand, our model seems to reproduce the three lines simultaneously. Since the free fall assumption needs to be adopted to reproduce the HCO^+ data, we therefore confirm that the original velocity structure of our models is better at reproducing the $C^{18}O$ observations and adds fewer free parameters. However, there could be other physical processes at work in the H_2O emitting region which mimic a multiple-step turbulence profile.

3.5. Discussion

3.5.1. Comparison with other studies

In general high-mass objects have higher turbulent velocities than their less massive counterparts. Whether this is a requirement for the initial conditions of high-mass star formation as suggested by McKee & Tan (2003) or whether the envelopes become more turbulent due to the

more energetic processes and surroundings is less clear. High-mass cores are more turbulent than their pre-stellar precursors (Jijina et al. 1999), and so must become more turbulent before the mid IR-quiet high-mass protostar phase and stay turbulent until at least the Ultra-Compact HII region phase given the consistent results obtained across the range of evolutionary stages present in the high-mass sample. Figure 3.5, *top-left*, is suggestive that the transition from the low- to the high-mass turbulent regime takes place at around $10^3 L_{\odot}$, though constraining this would need a much larger sample of sources which includes intermediate-mass YSOs covering a range of L_{bol} from 10^3 to $10^4 L_{\odot}$.

As introduced earlier, Herpin et al. (2012) presented a scenario in which turbulence increases with radius. They proposed that this result is in agreement with the turbulent core model (McKee & Tan 2003), and suggested that rotational motions and high density structures decrease the level of turbulence in the inner regions of the envelope. We justify the choice of a constant turbulent component as a function of radius by arguing that outflows inject turbulent motions into the envelope, especially in the inner parts, a scenario which can also be extrapolated to the low-mass protostars. Therefore, according to our models and results, the decay of turbulence due to density or other motions such as rotation or infall could be compensated with turbulence injected by the outflowing material and forces.

3.5.2. Origin of turbulence

There has been a debate for some time about the origin of the super-sonic turbulence observed towards molecular clouds and sites of low-mass star formation. Since this turbulence is expected to follow a Kolmogorov cascade, it should dissipate on timescales of the order of the free-fall timescale of a region if not driven (see e.g. Ballesteros-Paredes et al. 2007). As the lifetime of pre-stellar cores is typically 1.5–4 times the free-fall time (Ward-Thompson et al. 2007; André et al. 2014), any turbulence present due to the formation of the molecular cloud should have dissipated before the Class 0 phase. Indeed, the line-widths of many low-mass pre-stellar cores are consistent with little or no turbulence (e.g. Pineda et al. 2010). That we can rule out the no-turbulence model in our sources strongly suggests that the turbulence present in our sources is driven and sustained by the protostellar outflow.

Few confirmed massive starless cores have been found (Tackenberg et al. 2012; Tan et al. 2013), and this phase is expected to be short-lived compared to their free-fall time (Tackenberg et al. 2012). However, as in the low-mass case these have significantly lower line-widths (Jijina et al. 1999; Tan et al. 2013) than the protostellar sources studied here (see also Fig.12 of San José-García et al. 2013). It has been shown that in at least some cases outflows from high-mass star-forming regions have enough energy drive to turbulence on core scales (e.g. Mottram & Brunt 2012), therefore it seems likely that this is also the source of higher turbulence in our high-mass objects.

3.5.3. Turbulent core accretion and competitive accretion

In order to investigate if stars form from quasi-virial equilibrium cores, the constrained turbulent velocity derived from the best-fit RATRAN models, b_t , is compared to the virial velocity dispersion, σ_{vir} . This parameter is calculated from equation 2.8a of Bertoldi & McKee (1992) assuming that our sources are in virial equilibrium and afterwards converted to Doppler- b as:

$$\sigma_{\text{vir}} = \sqrt{\frac{\alpha_{\text{vir}} G M}{5 R}}, \text{ with} \quad (3.3)$$

$$b_{\alpha=1} = 0.6 \sigma_{\text{vir}} \sqrt{8 \ln(2)} \quad (3.4)$$

where the virial parameter α_{vir} is equal 1; the radius R inside of which the turbulence is measured is taken as the outer radius of our modelled envelope (r_{out} ; see Table 3.7); and M is the sum of the envelope mass inside that region and the calculated gravitational mass M_g . Regarding the choice of

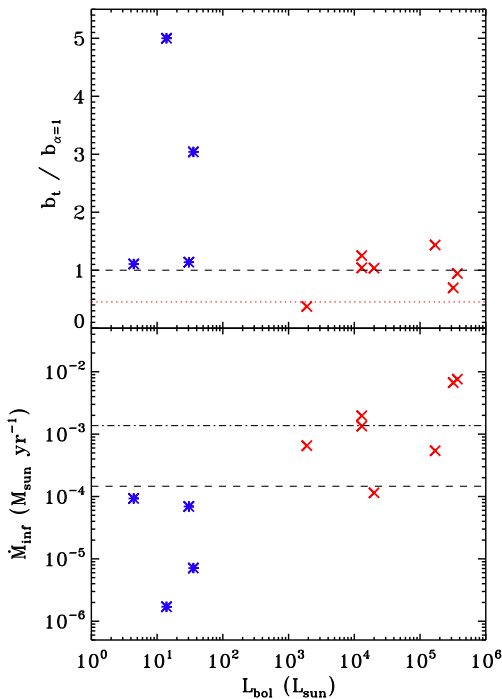


Figure 3.7: (*Top*) Ratio of the turbulent velocity b_t derived from the best-fit `RATRAN` mode and the virial velocity dispersion $b_{\alpha=1}$ as a function of bolometric luminosity of the source. The parameter $b_{\alpha=1}$ has been calculated for $R=r_{\text{out}}$ using equations 3.3 and 3.4. The dotted red line is the ratio obtained from a massive starless core presented in Tan et al. (2013). (*Bottom*) Instantaneous mass infall rate calculated assuming a minimum detectable infall radius at 1000 AU using equation 5 on Mottram et al. (2013) versus L_{bol} . The dashed black line indicates a typical value of the accretion rate in the core accretion model and the dotted-dashed black lines is the average accretion rate in the competitive accretion model (read Tan et al. 2014 for further discussion of these two theories). The blue asterisks correspond to low-mass protostars and the red crosses are the high-mass YSOs. Only the high-mass sources with negative infall velocity have been included.

R , we obtained consistent results for $b_{\alpha=1}$ when different values of the radius are used. The virial velocity of those sources with $v_r < 0 \text{ km s}^{-1}$ is presented in the last column of Table 3.5.

Our `RATRAN` models allow us to isolate the turbulent component and separate it from the other non-thermal motions that contributes to the broadening of the line profiles. Therefore, we can directly compare the actual turbulence contribution b_t to the velocity dispersion of a virialised system $b_{\alpha=1}$ and interpret the results in a more reliable framework than previously possible. The *top* panel of Fig. 3.7 shows the ratio of the turbulent velocity b_t and the calculated virial velocity $b_{\alpha=1}$ as a function of bolometric luminosity of the source. The dotted red line corresponds to a massive starless core (see Tan et al. 2013), where thermal motions prevail over non-thermal ones.

In the case of the low-mass protostars, the ratio is always greater than 1, suggesting that the level of turbulence is clearly larger than that expected in a system in virial equilibrium. For the high-mass YSOs this ratio fluctuates around 1 for six out of the seven sources. In general, the virialised line-width is slightly smaller than b_t , which indicates that the level of turbulence is also larger than in virial equilibrium sources. Therefore, according to the ratio and uncertainty associated to the constrained b_t , five massive stars form from a quasi-virial equilibrium core in which turbulence seems to prevail over the gravitational potential. This picture is consistent with current formation following the turbulent core accretion model proposed by McKee & Tan (2002, 2003). However, for the two remaining YSOs the ratio is smaller than 1, indicating that the level of turbulence is lower than that measure in a virialised system. These two sources (NGC6334-I(N), and G34.26+0.15), have the largest envelope masses of the studied sample and are known to reside in active regions forming multiple massive sources, where the large-scale gravitational potential may be more important. The current formation activity of these sources is therefore more similar to the competitive accretion model proposed by Bonnell et al. (1997).

According to the right-column panels of Fig. 3.5, the observed line width of the $\text{C}^{18}\text{O } J = 3-2$ data, i.e., the maximum turbulent velocity $b_{\text{max}(3-2)}$, is a factor ~ 1.5 larger than the constrained turbulent velocity from our best-fit models, b_t . This factor is even larger for the $\text{C}^{18}\text{O } J = 9-8$ transition. If we had used the observed line width to calculate the ratio showed in Fig. 3.7, most of the massive YSOs would be in the turbulent dominated regime. In addition, the virial parameter

derived from this assumed velocity dispersion would have been larger than 2, favouring the turbulent core accretion model over the competitive accretion. This result would agree with the typical values measured for α_{vir} in high-mass star-forming regions (see Heyer et al. 2009).

Therefore, the analysis of the turbulent component, which has been separated from the other non-thermal motions, suggest that both massive star formation theories can play a role on explaining the formation of massive stars.

Independently of the favoured model, in general a significant increase in turbulence is observed from the pre-stellar to protostellar phase, as already highlighted in Sect. 3.5.2 and pointed out by the dotted red line in Fig. 3.7. Only NGC6334-I(N) falls above that limit, corroborating that the region is really massive and has many YSOs associated, which creates a large gravitational potential that increase the virial velocity motion of the core. Given this increase in turbulence, it may be that all sources start out in a phase more like the competitive accretion model, but transition to something more like the turbulent core model when the outflow becomes active.

Finally, the *bottom* panel of Fig. 3.7 shows the instantaneous mass infall rate of each source as a function of its L_{bol} . The dashed and the dotted-dashed black lines indicate a typical value of the accretion rate in the core accretion model and the average accretion rate in the competitive accretion model, respectively. The expression to obtain these values are discussed in Tan et al. (2014), together with standard values of \dot{M}_{inf} characteristic of each formation theory. The mass infall rate is another way to discriminate between the core accretion and competitive accretion models. The reason is that in the former theory \dot{M}_{inf} is higher because the collapse is fed from a dense core while in the latter model is fed by a more diffuse clump.

In the case of the high-mass YSOs, the values of the mass infall rate are larger than $10^{-4} M_{\odot} \text{yr}^{-1}$, which are typical of those found in the turbulent core accretion model. However, in agreement with the previous discussion, our results seem to indicate that both models are at work and additional parameters besides the turbulent velocity and \dot{M}_{inf} are required to discriminate which theory explains more accurately the formation of these massive YSOs. It may even be the case that some combination of these two models is at work, with slow infall from the clump onto the core and faster infall on envelope scales.

3.5.4. Infall and rotation: disentangling the non-thermal emission

As noted in Sect. 3.1, rotation is another form of non-thermal motion that may play a role in the dynamical structure of protostellar envelopes, especially at small scales. Wang (2013) found that for high-mass objects the contribution of rotating regions to the total line width measured with single-dish telescopes is small and practically negligible on scales larger than 1000 AU. Similarly, Keto & Zhang (2010) found rotational velocities larger than 10 km s^{-1} only at radii closer than 600 AU for a $10 M_{\odot}$ star. In both cases, the regions in which rotation starts to be important are diluted within the beam of the HIFI and ground-based single-dish telescopes, so the contribution of this component to the measured line profile is negligible.

For the low-mass protostars, the physical scales probed by the HIFI beam are smaller than those of their massive counterparts (see Fig. 3.2). Harsono et al. (2013) showed that the contribution from a rotationally-supported disk (RSD) to integrated C^{18}O HIFI line fluxes is less than 10%. Harsono et al. (subm.) also computed line profiles from magneto-hydrodynamical simulations with and without a RSD, but without turbulence. Both the hydrodynamical models and the semi-analytic models neglecting turbulence show that the $\text{C}^{18}\text{O } J = 9-8$ line profiles are broadened by rotation, especially for high inclination ($i > 50^{\circ}$). Most of our low-mass sources are estimated to have $< 50^{\circ}$ inclination from outflow maps, however, except for IRAS2A (Yildiz et al., subm.). For this source, Brinch et al. (2009) concluded based on detailed interferometry that its velocity field is characterised by a high degree of infall relative to rotation. Therefore, rotation does not need to be considered for these five low-mass protostars but these studies demonstrate that rotation could contribute at a low level to the broadening of lines in low-mass sources, depending on the spatial resolution of the data.

To summarise, rotation does not contribute to the broadening of the observed HIFI C^{18}O data for any of the studied YSOs, a result which is consistent with our envelope models.

3.6. Conclusions

In this paper we have presented a combined analysis and `RATRAN` modelling of low- and high- J $C^{18}O$ and HCO^+ observations for a sample of low- and high-mass YSOs. The high- J $C^{18}O$ spectra obtained with HIFI trace the bulk of warm, dense and quiescent envelope gas on scales of 10^2 – 10^3 AU and 10^3 – 10^4 AU for each sub-group of objects respectively. Therefore, inner regions closer to the forming star which were not accessible with ground-based single-dish telescopes are now revealed. The results from this analysis suggest that the inner warm regions of the envelopes of low- and high-mass YSOs have similar dynamical properties while the outer colder parts present significant differences, particularly for the turbulent component and the abundance values. Other specific findings are:

- Pure infall dominated models can be ruled out for the entire sample of YSOs and pure turbulence dominated models can be excluded for more than 75% of our objects. Therefore, both turbulence and infall are required to reproduce and explain the $C^{18}O$ and HCO^+ spectra.
- Infall motions may be responsible for the broadening of the line-width of $C^{18}O$ with increasing J for low-mass protostars. Both rotation motions and a gradient in the turbulent component can be discarded as possible causes of the measured increase in the line-width for these studied low-mass sources.
- Turbulent motions are positively correlated with luminosity across the entire studied luminosity interval. On the scales probed by these observations (10^2 – 10^3 AU and 10^3 – 10^4 AU for low- and high-mass YSOs respectively), the turbulent Doppler-b typically ranges from 0.6 to 3.0 $km\ s^{-1}$ and remains constant across the envelope. Injection of turbulence by outflows is a plausible mechanism to explain the origin and sustenance of these motions.
- For high-mass YSOs, more luminous objects seem to have higher infall velocities over a larger fraction of envelope. In contrast, for low-mass YSOs the infall velocity is independent of source luminosity.
- The best-fit infall velocity is always smaller than the value derived from the estimated stellar mass for the high-mass objects. This result may imply that either the assumptions taken to calculate their stellar masses are too rough or that the infall cannot be as fast as free-fall due to the presence of high turbulence, rotation motions and/or counter-flows along the outflow cavity wall.
- Turbulence increases significantly from the pre-stellar to protostellar phase for both low- and high-mass objects. This results suggest that a source of turbulence, such as outflows, switches on during the actual star-formation process.
- The velocity dispersion derived from the turbulent velocity for most of the high-mass YSOs is of the order or larger than the dispersion associated to a system in virial equilibrium. Even if this picture is consistent with current formation following the turbulent core accretion model, the analysis of the isolated turbulent component suggests that both massive star formation theories can play a role on explaining the formation of high-mass stars.
- A jump abundance profile is needed to fit the high- J transitions of the $C^{18}O$ observations for the entire sample of YSO. Thus freeze out of CO is also necessary for high-mass objects with an evaporation temperature of ~ 35 K. The value of T_{eva} , higher than that measured in laboratory experiments with pure CO, indicates that CO ice is mixed with other ices such as CO_2 .

Acknowledgments

The authors thank Jonathan Tan and Ruud Visser for their comments and suggestions, which helped to improve the manuscript. Astrochemistry in Leiden is supported by the Netherlands Research School for Astronomy (NOVA) and by the European Community's Seventh Framework Programme FP7/2007-2013 under grant agreement 238258 (LASSIE). The James Clerk Maxwell Telescope is operated by the Joint Astronomy Centre on behalf of the Science and Technology Facilities Council of the United Kingdom, the National Research Council of Canada, and (until 31 March 2013) the Netherlands Organisation for Scientific Research. HIFI has been designed and built by a consortium of institutes and university departments from across Europe, Canada and the United States under the leadership of SRON Netherlands Institute for Space Research, Groningen, The Netherlands and with major contributions from Germany, France and the US. Consortium members are: Canada: CSA, U.Waterloo; France: CESR, LAB, LERMA, IRAM; Germany: KOSMA, MPIfR, MPS; Ireland, NUI Maynooth; Italy: ASI, IFSI-INAF, Osservatorio Astrofisico di Arcetri- INAF; Netherlands: SRON, TUD; Poland: CAMK, CBK; Spain: Observatorio Astronómico Nacional (IGN), Centro de Astrobiología (CSIC-INTA). Sweden: Chalmers University of Technology - MC2, RSS & GARD; Onsala Space Observatory; Swedish National Space Board, Stockholm University - Stockholm Observatory; Switzerland: ETH Zurich, FHNW; USA: Caltech, JPL, NHSC.

3.A. Best-fit models

3.A.1. Low-mass YSOs

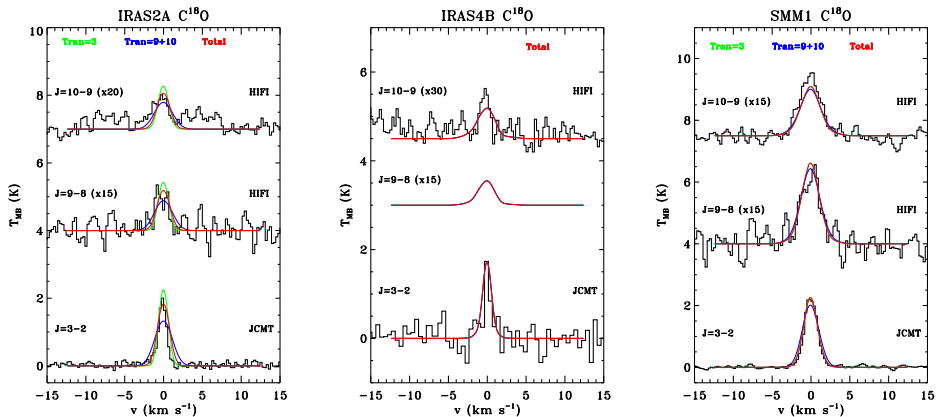


Figure 3.8: RATRAN models obtained for the low-mass Class 0 protostars NGC1333 IRAS2A, IRAS4B and Ser SMM1. The black lines show the observed spectra; the green line corresponds to the best χ_r^2 fit for the transition $J=3-2$; the blue line is the best χ_r^2 fit calculated from the HIPI spectra ($J=9-8$ and $J=10-9$); and finally the red line indicated the best χ_r^2 fit combining the three observations.

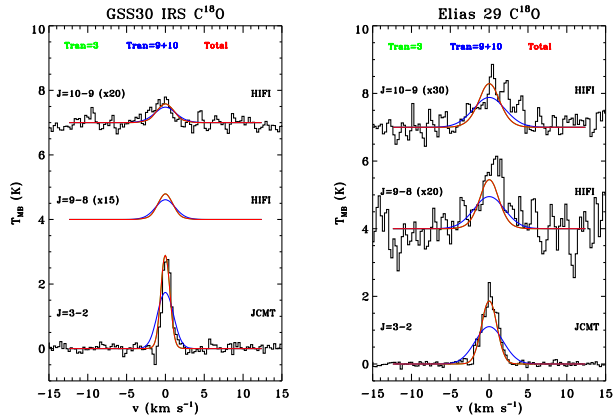


Figure 3.9: Same as Fig. 3.8 but for the low-mass Class I objects GSS30 IRS1 and Elias 29.

The high $C^{18}O$ abundance derived for Elias 29, which causes an unrealistic CO/H_2 ratio, could be a consequence of the low S/N of the high- J transition and therefore, the large uncertainty associated to the best-fit inner abundance, $X_i[C^{18}O]$, of this source. However, since Elias 29 is embedded in the Ophiucus PDR, the most plausible explanation of this extra emission is that the high- J $C^{18}O$ emission may arise partly in the warm extended gas. Lommen et al. (2008) concluded that a significant part of the molecular emission along the line of sight to Elias 29 is due to a density enhancement in the cloud ridge from which this source formed. Extended warm emission on large scales was not considered in the *DUSTY* calculations which defined the density and temperature structure used in our models, which may be the cause of the discrepant $X_i[C^{18}O]$ value obtained.

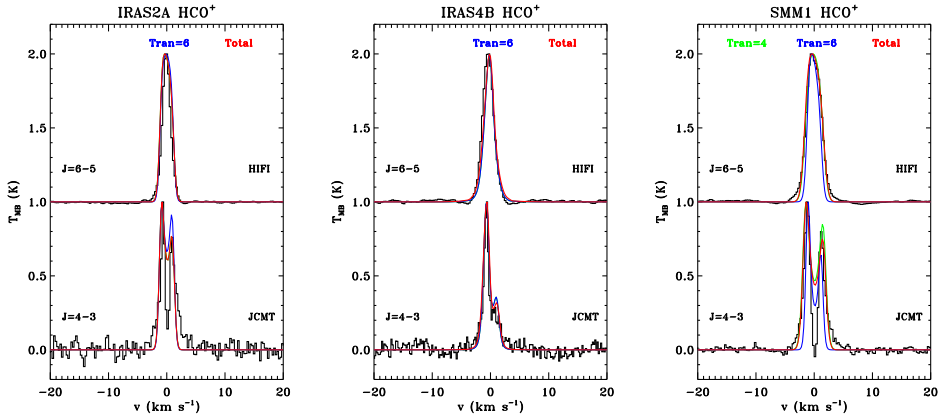


Figure 3.10: Normalised RATRAN models obtained for HCO^+ for the low-mass Class 0 protostars NGC1333 IRAS2A, IRAS4B, and Ser SMM1 compared to the normalised observations, shown in black. The green line corresponds to the best χ_r^2 fit for the transition $J=4-3$; the blue line is the best χ_r^2 fit for the $J=6-5$ line, if presented; and finally the red line indicates the best χ_r^2 fit combining the available observations.

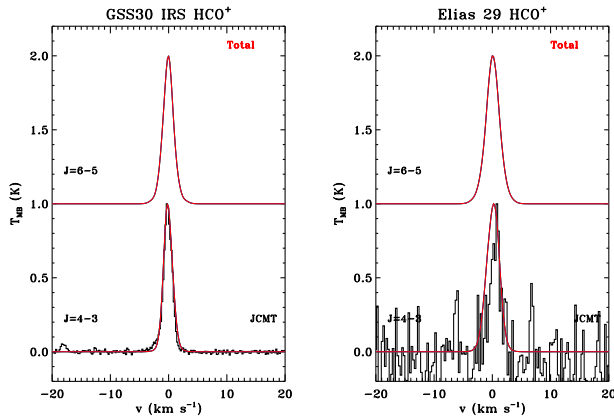


Figure 3.11: Same as Fig. 3.10 but for the Class I protostar GSS30 IRS1 and Elias 29.

The derived value of $X_1[^{12}\text{CO}]$ presented in the latter column of Table 3.3 is an order of magnitude higher than for the other sources. Therefore, this source is excluded from the average calculation of the C^{18}O , ^{12}CO and HCO^+ abundance profiles presented in Table 3.4.

3.A.2. High-mass YSOs

It is difficult to reproduce the large intensity observed in the C^{18}O lines towards some high-mass sources, resulting in the need for high C^{18}O abundances. In the case of NGC6334-I(N), the models always underestimate the $J = 10-9$ line, regardless of the chosen value of $X_1[\text{C}^{18}\text{O}]$. The $J = 9-8$ transition is reproduced and the $J = 3-2$ line is not available for this object, so we cannot extend the comparison to colder regions of the envelope. A possible reason why the higher- J spectrum cannot be recreated could be due to the ripples in the baseline of these transitions, which increases the intensity of the line by creating additional and artificial broad line wings. The ripples are present in the entire spectrum and are difficult to eliminate with lineal-baseline subtraction techniques, becoming even more complicated due to the low S/N of the line. Therefore, for this source we prioritise the fitting of the $J = 9-8$ transition over the global one to constrain the

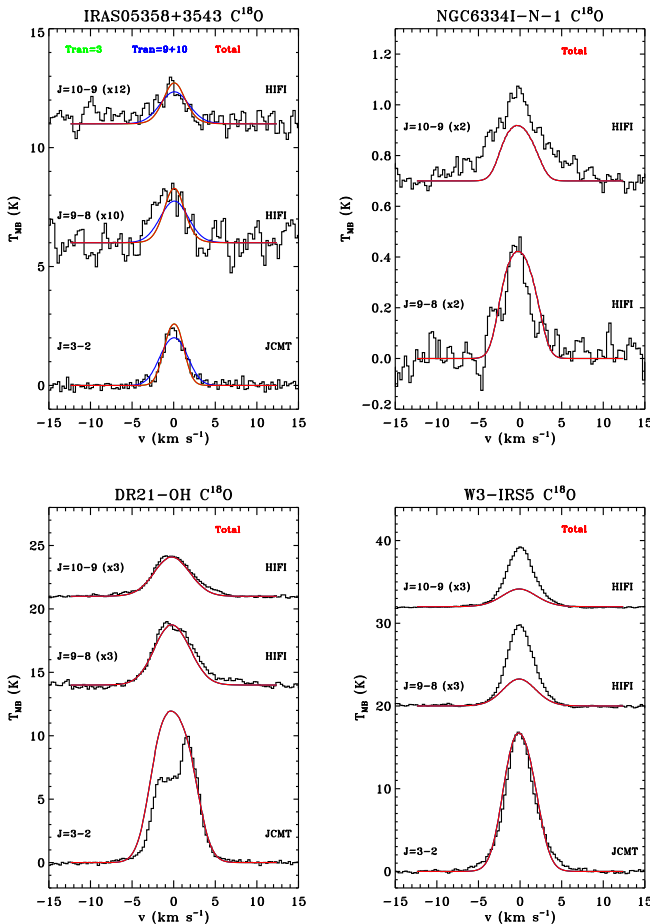


Figure 3.12: RATRAN models obtained for the high-mass sources IRAS05358+3543, DR21(OH), NGC6334-I(N), and W3-IRS5. The black lines show the observed spectra; the green line corresponds to the best χ_r^2 fit for the transition $J=3-2$; the blue line is the best χ_r^2 fit calculated from the HIFI spectra ($J=9-8$ and $J=10-9$); and finally the red line indicated the best χ_r^2 fit combining the three observations.

$C^{18}O$ “jump abundance profile” and the turbulent component. For the HCO^+ observations, both abundance and infall velocity are well fit.

A high value of $X_i[C^{18}O]$ is needed in order to fit the $C^{18}O$ observations of W3-IRS5, which implies a CO/H_2 ratio $> 2.7 \times 10^{-4}$. In this case, the HIFI spectra have high S/N , so this result cannot be justified by adding a large uncertainty to the abundance value. On the other hand, this YSO is well known for being massive, luminous, with powerful outflows and with at least two main objects dominating the emission (read Chavarría et al. 2010 for more information about the source). Therefore, the complexity of this object may not be well represented by the assumed envelope structure modelled with RATRAN leading to some disagreement between even the best-fit model and the observations.

Finally, a particular case to highlight is G34.26+0.15. Looking at the $C^{18}O$ data, an emission peak at $\sim 4 \text{ km s}^{-1}$ is observed in both low- and high- J transitions. Therefore, we assumed that this bump, which is especially visible in the $J=3-2$ line, is caused by foreground emission. In the case of the HCO^+ $J=4-3$ spectrum, since the emission is located at slightly larger velocities with respect the source velocity, we have assumed this is part of the double-peak profile of the HCO^+ data.

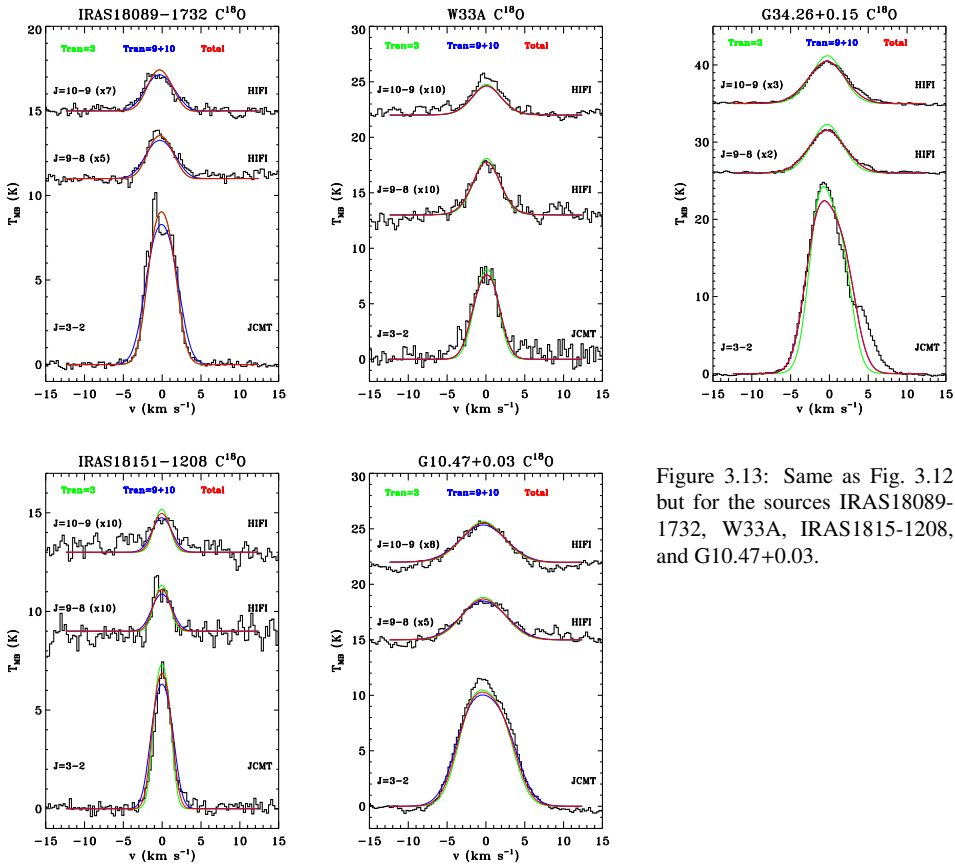


Figure 3.13: Same as Fig. 3.12 but for the sources IRAS18089-1732, W33A, IRAS1815-1208, and G10.47+0.03.

3.B. Additional information and figures

The skewness and blue and red peak intensity ratio of the HCO^+ $J = 4-3$ spectra are measured for each YSOs and presented in Table 3.6. These two parameters, which characterise the asymmetry of a line profile, are also calculated for the best-fit RATRAN models in order to compare these resulting profiles to the observations.

In Table 3.7 is shown the input parameters used in our RATRAN models and described in Sect. 3.3.1.

In addition, further details regarding the iteration technique explained in Sect. 3.3.3 and developed to constrain the best-fit models are presented in Sect. 3.B.1.

Finally, figures showing the output line profiles obtained from RATRAN models with really high infall velocities (Sect. 3.4.1) and different envelope structure as explained in Sect. 3.4.2 are shown below.

3.B.1. Iteration technique: details

The main steps of the procedure which constrains the contribution of the infall and turbulence motions, v_r and b_t , to the HCO^+ and C^{18}O line profiles are described in Sect. 3.3.3. However, technical details explaining how the reduced χ_r^2 value for each model is calculated are not indicated in that section in order to simplify it and to focus the attention on the purpose and goal of each step.

As indicated, the best-fit models of each source and molecule are those with the lowest χ_r^2 , calculated considering the specific number of degrees of freedom. In general, the procedure to derive this quantity, and therefore to compare observations and models, is similar regardless of the

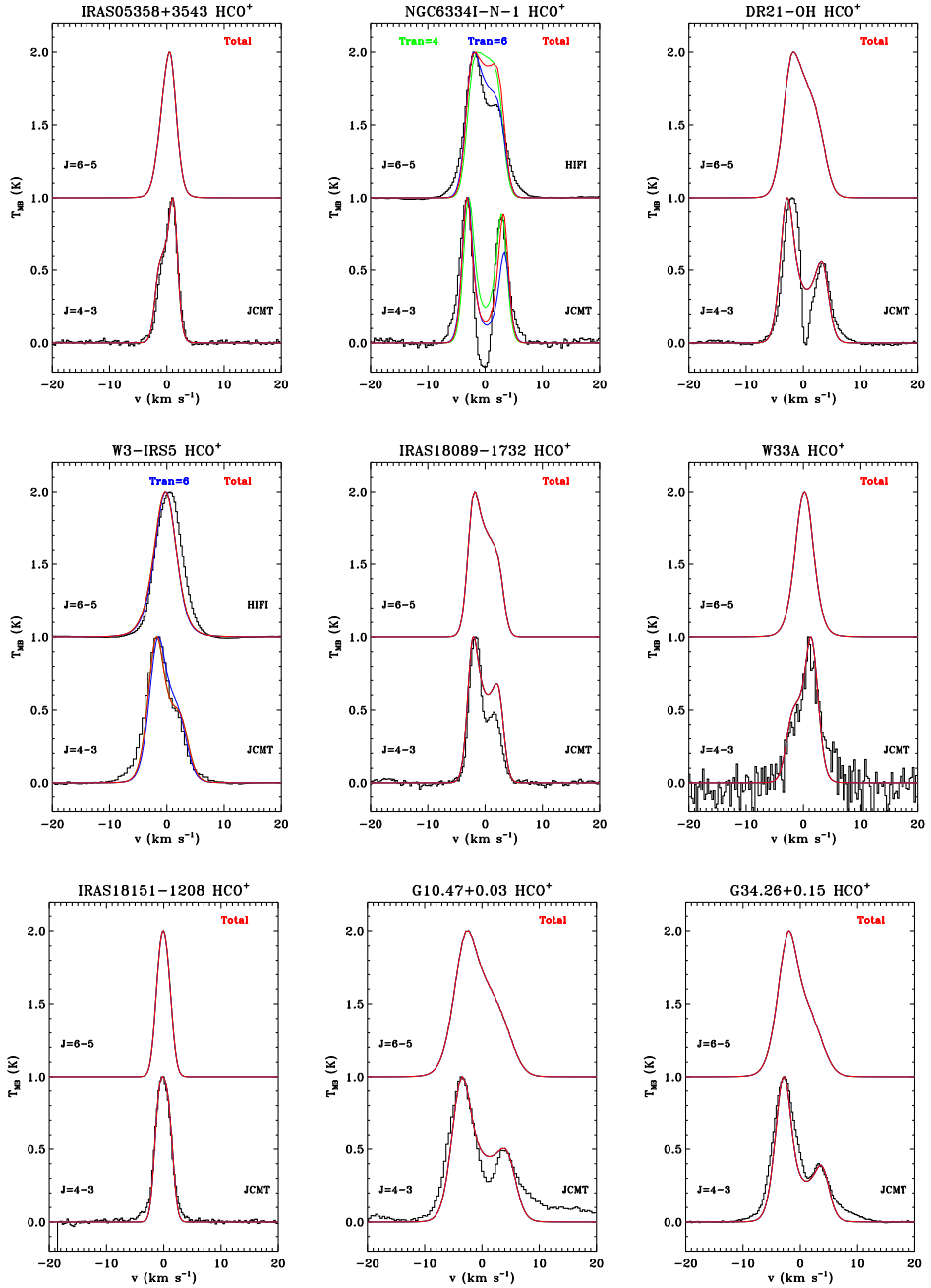


Figure 3.14: Same as Fig. 3.10 but for the high-mass YSOs IRAS05358+3543, NGC6334-I(N), DR21(OH), W3-IRS5, IRAS18089-1732, W33A, IRAS1815-1208, and G34.26+0.15, and G10.47+0.03.

Table 3.6: Skewness and the blue and red peak intensity ratio of the $\text{HCO}^+ J = 4-3$ modelled and observed line profile.

Source	Skewness ^a Mod.	T_B/T_R Mod.	Skewness ^a Obs.	T_B/T_R Obs.
Low-mass				
NGC1333 IRAS 2A	-0.13	1.3	-0.18	1.3
NGC1333 IRAS 4B	-0.47	2.8	-0.62	3.5
Ser SMM1	-0.18	1.3	-0.18	1.3
GSS30 IRS1	-0.20	1.0	-0.27	1.0
Elias 29	0.18	1.0	0.53	1.0
High-mass				
IRAS05358+3543	0.23	1.0	0.39	1.0
NGC6334-I(N)	-0.07	1.1	-0.06	1.2
DR21(OH)	-0.30	1.8	-0.24	1.7
W3-IRS5	-0.36	1.0	-0.44	1.0
IRAS18089-1732	-0.22	1.5	-0.36	2.0
W33A	0.32	1.0	0.33	1.0
IRAS18151-1208	-0.05	1.0	-0.03	1.0
G10.47+0.03	-0.36	2.0	-0.33	2.0
G34.26+0.15	-0.51	2.6	-0.57	2.5

Notes. ^(a) Skewness measured in the interval $v_{\text{LSR}} \pm 1.25 \text{ km s}^{-1}$ for low-mass protostars and $v_{\text{LSR}} \pm 3.5 \text{ km s}^{-1}$ for high-mass YSOs according to equation 1 of Gregersen et al. (1997).

Table 3.7: Overview of the main parameters of the physical model of each source: exponent of the power-law $n \propto r^{-p}$, and radius, density and temperature of the inner and outer regions of the modelled envelope.

	p	r_0 (AU)	n_0 (cm^{-3})	T_0 (K)	r_{out} (AU)	n_{out} (cm^{-3})	T_{out} (K)
Low-mass							
NGC1333 IRAS 2A	1.7	35.9	4.9(8)	235	1.7(4)	1.4(4)	10
NGC1333 IRAS 4B	1.7	15.0	2.0(9)	240	3.8(3)	8.7(5)	10
Ser SMM1	0.8	31.0	3.8(8)	232	1.2(4)	1.7(5)	10
GSS30 IRS1	2.0	16.2	1.2(8)	239	6.0(3)	1.1(4)	15
Elias 29	2.0	15.5	6.5(7)	243	3.8(3)	1.1(4)	18
High-mass							
IRAS05358+3543	1.5	30.0	1.5(9)	1183	5.4(4)	2.0(4)	17
NGC6334-I(N)	1.3	30.0	6.0(9)	1381	7.2(4)	2.4(5)	11
DR21(OH)	1.4	50.0	1.0(9)	1296	5.0(4)	6.5(4)	20
W3-IRS5	1.4	70.0	2.1(8)	1279	11.3(4)	1.1(4)	29
IRAS18089-1732	1.9	100.0	4.0(9)	1435	3.9(4)	4.7(4)	22
W33A	1.2	60.0	2.5(8)	1137	7.1(4)	5.2(4)	19
IRAS18151-1208	1.4	30.0	9.3(8)	1108	5.0(4)	2.9(4)	19
G10.47+0.03	1.4	100.0	9.8(8)	1237	6.0(4)	1.3(5)	29
G34.26+0.15	1.4	160.0	4.6(8)	1411	8.1(4)	7.6(4)	27

parameter (abundance, v_r or b_t) to be constrained. However, there are some differences concerning the calculation of the reduced χ_r^2 between the HCO^+ and C^{18}O observations.

In the case of the HCO^+ lines, the value of χ_r^2 for each output image is obtained by interpolating the model profiles to the same spectral resolution of the observations, normalising both model and observation to their peak intensities, and comparing then the line intensity channel-by-channel. This method was chosen because the priority of this study is to fit the shape of the spectra rather than the intensity since infall/expansion and turbulence dominated profiles have different shapes.

With this method, the best-solutions normally agree with what is also considered a good match between observation and models by visual inspection. The blue/red ratio of the double peak profile and the skewness of the $J = 4-3$ line are measured for the RATRAN models and compared to those calculated for the observations (see Table 3.6). In the selection of the best-fit, we prioritise the fitting of the HCO^+ $J = 4-3$ line because, as introduced in Sect. 3.3.4, the HCO^+ $J = 6-5$ line is always underestimated by our RATRAN models.

For the C^{18}O spectra, the models are also interpolated to the same spectral resolution as the available observations. Then, χ_r^2 is calculated comparing also the line intensity channel-by-channel, but this time without normalising the spectra and models. The reason is that C^{18}O is optically thin, which makes the abundance easier to constrain. As a sanity check, the solutions within one sigma uncertainty are also examined by visual inspection. In addition, for this molecule, χ_r^2 values are calculated globally, i.e., considering all the available lines, and separately for the low- J (JCMT/APEX data) and the high- J (HIFI $J = 9-8$ and $J = 10-9$) spectra, modifying accordingly the degrees of freedom in each case. The purpose is to compare the best solution between different parts of the envelope (at inner and outer radii) with the global best-fit to contrast the results.

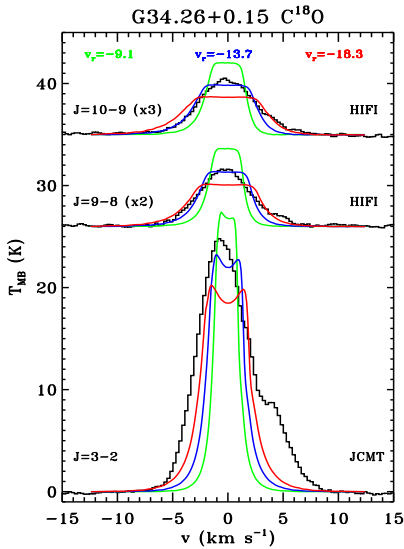


Figure 3.15: Comparison between infall-dominated models ($b_t=0.0 \text{ km s}^{-1}$) with the same abundance profile but with different values of infall velocities at 1000 AU. The green, blue, and red profiles correspond to RATRAN models with $v_{r=1000 \text{ AU}}$ equal to -9.1 km s^{-1} , -13.9 km s^{-1} , and -18.3 km s^{-1} respectively. The black line shows the observed spectra.

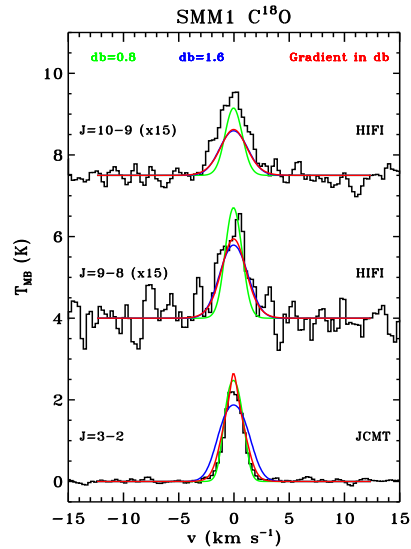


Figure 3.16: RATRAN model of the low-mass Class 0 protostars Ser SMM1. The black lines indicate the observed spectra; the green line corresponds to the model with a constant turbulent velocity $b_t=0.8 \text{ km s}^{-1}$; the blue the RATRAN image with a constant $b_t=1.6 \text{ km s}^{-1}$; and finally the red line is the model for which b_t was decreased at larger distances from the central position. For these three models, the infall velocity field is the same ($v_{r=1000 \text{ AU}}=-0.3 \text{ km s}^{-1}$).

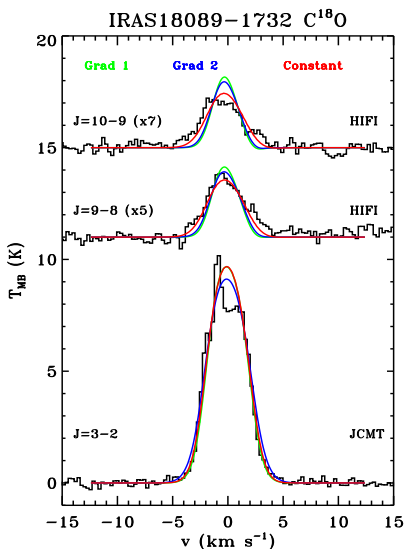


Figure 3.17: RATRAN model of the high-mass YSO IRAS18089. The observed spectra are plotted in black while the models with increasing turbulence with radius are in green and blue. The gradient of b_t is steeper for the blue model, resulting in broader profiles. The red line corresponds to the best-fit model with constant turbulent motions. For these three models, free fall is assumed ($v_{r=1000 \text{ AU}}=-0.3 \text{ km s}^{-1}$).

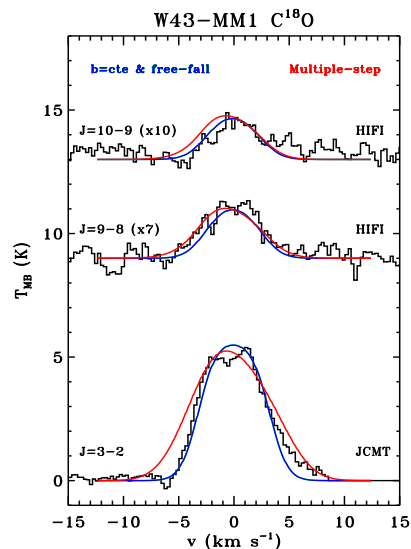


Figure 3.18: RATRAN model of the high-mass YSO W43-MM1 compared to the observed spectra in black. The blue model is generated assuming free fall and constant turbulence while the red profiles are obtained using the "multiple-step profile" presented by Herpin et al. (2012). The same C^{18}O abundance is assumed for both models.